HHS Public Access

Author manuscript

Nat Metab. Author manuscript; available in PMC 2025 March 10.

Published in final edited form as:

Nat Metab. 2024 July ; 6(7): 1347–1366. doi:10.1038/s42255-024-01078-9.

PAQR4 regulates adipocyte function and systemic metabolic health by mediating ceramide levels

Qingzhang Zhu[1], **Shiuhwei Chen**[1], **Jan-Bernd Funcke**[1], **Leon G. Straub**[1], **Qian Lin**[1], **Shangang Zhao**[1,2], **Chanmin Joung**[1], **Zhuzhen Zhang**[1], **Daeseok Kim**[1], **Na Li**[1], **Christy Gliniak**[1], **Charlotte Lee**[3], **Alberto Cebrian-Serrano**[4,5], **Line Pedersen**[1,6], **Nils Halberg**[6], **Ruth Gordillo**[1], **Christine M. Kusminski**[1], **Philipp E. Scherer**[1,*]

[1]Touchstone Diabetes Center, Department of Internal Medicine, University of Texas Southwestern Medical Center, Dallas, TX, USA

[2]Sam and Ann Barshop Institute for Longevity and Aging Studies, Division of Endocrinology, Department of Medicine, University of Texas Health Science Center at San Antonio, San Antonio, TX, 78229, USA.

[3]Center for Hypothalamic Research, University of Texas Southwestern Medical Center, Dallas, TX, USA

[4]Institute for Diabetes and Obesity, Helmholtz Zentrum München, Munich, Germany

[5]German Center for Diabetes Research (DZD), Neuherberg, Germany

[6]Department of Biomedicine, University of Bergen, Bergen, Norway

Summary

PAQR4 is an orphan receptor in the PAQR family with unknown function in metabolism. Here, we unveil a critical role of PAQR4 in maintaining adipose tissue function and whole-body metabolic health. We demonstrate that expression of *Paqr4* specifically in adipocytes, in an inducible and reversible fashion, leads to partial lipodystrophy, hyperglycemia, and hyperinsulinemia, which is ameliorated by wildtype adipose tissue transplants or leptin treatment. In contrast, deletion of *Paqr4* in adipocytes improves healthy adipose remodeling and glucose homeostasis in diet-induced obesity. Mechanistically, PAQR4 regulates ceramide levels by mediating the stability of ceramide synthases (CERS2 and 5), and thus their activities. Overactivation of the PQAR4-CERS axis causes ceramide accumulation and impairs adipose tissue function through suppressing adipogenesis and triggering adipocyte de-differentiation. Blocking *de novo* ceramide biosynthesis rescues PAQR4-induced metabolic defects. Collectively, our findings suggest a critical function of PAQR4 in regulating cellular ceramide homeostasis and targeting PAQR4 offers an approach for the treatment of metabolic disorders.

[*]Correspondence: philipp.scherer@utsouthwestern.edu.

Author Contributions

Q.Z and P.E.S conceptualized the study and designed experiments. Q.Z., S.C., J.F., L.G.S., Q.L., S.Z., C.J., Z.Z., D.K., N.L., C.G., C.L., R.G., C.M.K. conducted experiments and A.C.-S. was involved in the generation of the floxed mice. N.H., L.P. and C.M.K. were involved in study design and data flow in the paper. All authors analyzed and interpreted data. Q.Z. wrote the manuscript and C.M.K. and P.E.S revised it.

Declaration of Interests

The authors declare no competing interests.

Introduction

The ability of adipose tissue to dynamically adapt to various nutritional conditions is center stage to the preservation of metabolic homeostasis[1,2]. An unhealthy expansion of adipose tissue during obesity, mainly via a process referred to as hypertrophy (*i.e.* an increase in adipocyte size) rather than hyperplasia (involving *de novo* adipogenesis), is closely tied to chronic inflammation in adipose tissue, dyslipidemia, and systemic insulin resistance. However, adipose tissue atrophy or lipodystrophy (pathological conditions featuring a loss of fat tissue) are also associated with whole-body metabolic dysfunction due to aberrant lipid accumulation in non-adipose tissues and lower levels of critical adipokines, such as leptin and adiponectin. Moreover, adipocyte de-differentiation has recently been observed in several (patho)physiological settings, including lactation[3], skin repair and fibrosis[4,5], as well as several types of cancer, such as liposarcomas[6], nasopharyngeal carcinoma[7], and breast cancer[8]. Thus, further insights into the mechanisms underlying adipose tissue remodeling are critical for a basic understanding of adipose tissue function and the associated metabolic dysregulation.

Sphingolipids are initially generated by the condensation of palmitoyl-CoA and serine through the enzyme serine palmitoyltransferase (SPT). Ceramides are key players in sphingolipid metabolism, as they are the foundation for the synthesis of more complex sphingolipids such as sphingomyelins and lactosylceramides. Increased ceramide levels are tightly linked to cellular dysfunction in different tissues. Inhibiting ceramide biosynthesis in adipocytes enhances adipose tissue beiging and improves adipose tissue metabolism in a cell-autonomous way[9]. Accordingly, numerous studies suggest that sphingolipids are closely associated with multiple pathophysiological conditions, including insulin resistance, type 2 diabetes, cardiovascular complications, and cancer[10,11]. Moreover, genetic or pharmacological inhibition of *de novo* ceramide synthesis ameliorates glucose intolerance and insulin resistance in obese and diabetic models with dyslipidemia[12] suggesting that such lipotoxic consequences are, at least in part, associated with these sphingolipid species. However, we have a limited understanding of the detailed mechanistic basis as to how a cell maintains ceramide levels.

The progestin and adipoQ receptor (PAQR) family features proteins with seven transmembrane helices and contains eleven sequence paralogs in three classes, with apparently distinct agonist specificities[13,14]. Class I includes PAQR1 through PAQR4. Amongst the members of this group, PAQR1 and 2 are well-known as adiponectin receptors (AdipoR1 and 2). They play an important role in obesity-associated metabolic diseases and cancer[15]. Adiponectin, an insulin-sensitizing adipokine, effectively lowers ceramide levels by stimulating a ceramidase activity within AdipoR1/2[16]. In contrast to AdipoR1/2 and PAQR3, PAQR4 is not responsive to adiponectin[17]. Moreover, PAQR4 does not appear to be a plasma membrane receptor, as it mainly localizes to the Golgi apparatus[18]. This suggests it may not act as a ‘classical receptor’ involved in signal transduction from the extracellular milieu, such as AdipoR1/2. Likewise, PAQR3 acts as an anchor protein for Scap/SREBP in the Golgi and regulates cholesterol homeostasis[19]. PAQR3 also serves as a tumor suppressor in different cancer types[20,21], whereas PAQR4 seems to promote tumor progression, likely

by regulating cell cycle and/or local ceramide toxicity[18,22]. Thus, PAQRs may play powerful roles in distinct biological processes. Importantly, these proteins are potential therapeutic targets, as exemplified by AdipoR1/2 modulators developed to address metabolic diseases and cancer[23]. However, the closest homolog to AdipoR1/2, which is PAQR4, remains an understudied member beyond its tumor-associated effects. Here, by using an array of mouse models with both gain- and loss-of-function, we demonstrate that PAQR4 acts as an essential regulator of adipocyte function, critically involved in ceramide metabolism, thereby impacting global metabolic homeostasis. Based on our findings, PAQR4 may serve as a powerful therapeutic target for metabolic diseases.

Results

PAQR4 is an important player in regulating adipose function

Adipose tissue dysfunction is an important component and frequently a driving force for metabolic disorders. *PAQR4* expression is upregulated in abdominal subcutaneous adipose tissue (sWAT) in obese patients, associated with fibrogenesis[24], regardless of the degree of impaired glucose metabolism, compared to healthy lean sWAT (Fig. 1a). The upregulation of *PAQR4* is inversely correlated with the decrease of *ADIPOQ* and *PPARG* expression, suggesting an important role in adipose tissue remodeling (Fig.1a–b). Likewise, in an unbiased gene expression analysis by RNA-Seq[25,26], *Paqr4* was identified as a top hit with remarkable upregulation in widely expanded adipose tissues, including gonadal (gWAT), inguinal (sWAT), mesenteric white adipose tissue (mWAT), and brown fat (BAT) from massively obese mice, compared to less expanded adipose tissues from obese mice, in both males and females (Extended Data Fig.1a–b). *Paqr4* was most abundant in WAT and heart tissue when examining multiple tissues (Extended Data Fig. 1c). However, *Paqr4* upregulation in response to high-fat diet (HFD)-exposure was observed in adipose tissues but not in the heart (Extended Data Fig.1d), indicating a special role in adipose tissue function. Little is known about the metabolic function of PAQR4. We therefore generated transgenic mice that allowed us to express *Paqr4* specifically in adipocytes in a doxycycline (dox)-dependent manner (hereafter referred to as Paqr4^{ad} mice) (Fig.1c). Upon dox treatment, *Paqr4* was only induced in adipose tissues, but not in other tissues (Extended Data Fig.1e), highlighting the tissue specificity of our system. Upon induction on dox-chow, Paqr4^{ad} mice displayed a remarkable decrease in body weight (Fig. 1d–e), mainly due to a reduction in fat mass (Fig. 1f–g). In contrast, lean mass was increased (Extended Data Fig.1f–g), consistent with a lipodystrophic phenotype. Indeed, weight, volume and size of the various fat pads were markedly reduced, whereas the liver was massively steatotic (Fig. 1h–i; Extended Data Fig.1h–i; Supplementary movie 1–2). Moreover, histological analyses reflected enhanced macrophage infiltration and fibrosis in adipose tissues and more lipid accumulation in the liver (Fig. 1j). The impact of *Paqr4* overexpression in the adipocytes occurred rapidly. Expression of genes related to adipogenesis and mature adipocytes were significantly downregulated (Fig. 1k), together with decreases in circulating adiponectin and leptin levels (Fig. 1l–m), all within one week of gene induction. Thus, PAQR4 overexpression caused severe fat degeneration. As a result of fat loss, Paqr4^{ad} mice displayed hypothermia upon acute and adapted cold exposure (Fig.1n; Extended Data Fig.1j). Moreover, Paqr4^{ad} mice exhibited glucose intolerance and impaired insulin-

mediated glucose disposal within 2–3 weeks of dox-chow induction (Extended Data Fig.1k–m), both of which were further aggravated thereafter (Fig. 1o–q). Therefore, adipocyte PAQR4 plays an important role in adipose tissue function.

PAQR4 induces insulin resistance despite weight loss

We more specifically addressed the role of PAQR4 in diet-induced obesity. Consistent with the results observed under chow-fed conditions, in a dox dose-dependent manner (Extended Data Fig.2a), HFD-fed Paqr4^{ad} mice displayed a substantially reduced weight gain, mainly due to a reduction in fat mass, as well as severe hepatic steatosis with elevated ALT levels (Fig.2a–e; Extended Data Fig.2b–g). Moreover, within 2 weeks of dox-HFD feeding, Paqr4^{ad} mice exhibited remarkably reduced respiratory exchange ratios (RER) under both fed and refed conditions, which were not altered upon overnight fasting (Extended Data Fig.2h). This is reflective of a dramatically reduced metabolic flexibility in these mice. Thus, PAQR4 caused a shift from carbohydrate oxidation towards fat oxidation, with carbohydrate oxidation being reduced during feeding as well as upon refeeding after a fast. In fact, carbohydrate use was maintained at constant levels during fasting as under fed conditions (Extended Data Fig.2i). In contrast, fatty acid oxidation was elevated both in the fed state as well as upon refeeding after a fast. During fasting, fatty acid oxidation remained at the same level as in the fed state (Extended Data Fig.2j). VO_2, VCO_2 and energy expenditure (EE) were slightly reduced under fed conditions, whereas physical activity was unaltered (Extended Data Fig.2k–n). Moreover, there was no impact on food intake during this time period when body weight differences were very small (Extended Data Fig.2o). Thus, PAQR4 regulates metabolic homeostasis by dramatically altering metabolic flexibility rather than food intake.

Histological analyses demonstrated enhanced macrophage infiltration in Paqr4-transgenic adipose tissues (Fig.2e; Extended Data Fig.3a). In addition, gene expression analyses revealed that anti-inflammatory M2 macrophages were increased in both in gWAT and sWAT, concomitant with a suppression of some pro-inflammatory cytokines, such as *Il1b* and *Il6*, but not *Tnf* (Fig.2f–g). Both M1 and M2 macrophages were elevated in BAT (Extended Data Fig.3a–b). Moreover, fibrosis was markedly enhanced in all fat pads, including gWAT, sWAT, and BAT from Paqr4^{ad} mice (Extended Data Fig.3c). Consistent with the impaired adipose tissue function, lower circulating adiponectin and leptin levels were observed (Fig.2h–i), concomitant with hyperglycemia and hyperinsulinemia (Extended Data Fig.3d–e), in a dox-dose dependent manner. As a consequence, Paqr4^{ad} mice displayed glucose intolerance and impaired insulin-mediated glucose disposal upon 2–3 weeks of dox-HFD feeding (Extended Data Fig.3f–g) and this impairment was massively aggravated at later time points (Fig.2j–m, Extended Data Fig.3h–i). As compared to chow-fed conditions, where glucose-stimulated insulin release was elevated in Paqr4^{ad} mice, the effect was substantially decreased under HFD-fed conditions (Fig.2k–l). Massive β cell hypertrophy was observed in the pancreas of Paqr4^{ad} mice, albeit with overall less insulin content (Fig.2e), indicating impaired β cell function. In addition, insulin signaling was impaired in multiple metabolic tissues (Extended Data Fig.3j–k).

Therefore, when *Paqr4* expression is initiated at the onset of obesogenic conditions and maintained using dox-HFD, PAQR4 reduces adiposity but impairs glucose homeostasis. We thus asked whether these effects would still occur if we induce *Paqr4* gene expression in mice with pre-existing obesity. We pushed the mice to an obese state with 6-weeks of HFD only (without dox supplementation), and then switched to dox-HFD. Interestingly, even under these conditions, induction of *Paqr4* not only prevented further weight gain, but caused rapid weight loss, along with lower circulating leptin levels and impaired glucose tolerance (Fig.2n–q). These findings indicate that PAQR4 exerts its potent effects on the adipocyte even in the obese state.

Amelioration of PAQR4-induced metabolic defects by fat transplants or leptin

Given that PAQR4 overexpression causes lipodystrophy, we next asked whether an adipose tissue transplant from a wildtype mouse would improve the metabolic state. To this end, we transplanted sWAT from control mice to the corresponding sites of Paqr4^{ad} mice. The transplants grew well in Paqr4^{ad} mice fed with dox-chow, in sharp contrast to the atrophic endogenous sWAT (Fig.3a–b). Interestingly, the transplants fully reversed hyperglycemia and hyperinsulinemia in Paqr4^{ad} mice (Fig.3c–d). Accordingly, glucose tolerance and insulin-mediated glucose disposal were also normalized (Fig.3e–g). However, the overall body weight loss and the fatty liver phenotype were not rescued (Extended Data Fig.4a–c). Furthermore, the transplants did not normalize circulating leptin and adiponectin levels (Fig.3h; Extended Data Fig.4d). In fact, leptin levels were even further reduced upon transplantation.

Leptin constitutes a treatment option for lipodystrophy in humans. In light of the partial lipodystrophy prevailing in the transgenic mice, we decided to infuse Paqr4^{ad} mice that were fed with 14-weeks of dox-chow with a physiological leptin dose (Fig.3i), which doubled the circulating levels in the transgenic mice. At this dose, leptin did not rescue body weight or fat mass (Extended Data Fig.4e–f), and it also had only minimal effects on food intake (Extended Data Fig.4g). However, leptin treatment improved hyperglycemia and hyperinsulinemia both under fed and fasted conditions (Fig.3j–k). Leptin treatment moreover mitigated liver steatosis, reflected by a decreased liver/body weight ratio, liver triglyceride content, and serum ALT levels (Fig.3l–n; Extended Data Fig.4h). In addition, glucose tolerance and insulin tolerance were normalized by leptin treatment (Fig.3o–p). Interestingly, leptin infusion also improved the histological appearance of adipose tissue (Extended Data Fig.4h), and slightly increased circulating adiponectin levels (Fig.3q), suggesting that leptin supplementation partially improves metabolic stress in the adipose tissues of Paqr4^{ad} mice.

We also crossed the Paqr4^{ad} mice into the leptin-deficient *ob/ob* background. Interestingly, *ob/ob:*Paqr4^{ad} mice gained substantially less body weight than their *ob/ob* controls (Extended Data Fig.4i). Notably, food intake was transiently reduced by PAQR4 assessed at the beginning of dox-induction when body weight was similar. However, it recovered to control levels soon thereafter, both in Paqr4^{ad} and *ob/ob:*Paqr4^{ad} mice (Extended Data Fig.4j). Surprisingly, glucose intolerance was even more severe in *ob/ob:*Paqr4^{ad} mice than in *ob/ob* mice, although glucose-stimulated insulin levels were comparable (Extended Data

Fig.4k–l). Thus, Paqr4-induced adipose tissue dysfunction occurs even in the complete absence of leptin. Paqr4^{ad} mice, therefore, do not exert their effects on metabolism through leptin; however, leptin is clearly able to improve the insulin resistance induced by *Paqr4* overexpression.

Paqr4-deletion in adipocytes improves glucose homeostasis in obesity

As the overexpression of *Paqr4* in adipocytes clearly exerts detrimental effects, we also wanted to investigate the consequences of a loss of function of the *Paqr4* gene in adipocytes. We generated Paqr4-flox mice and crossed them with Adipoq-rtTA and TRE-Cre mice to achieve a dox-dependent, inducible knockout of *Paqr4* specifically in adipocytes (hereafter referred to Paqr4^{iAKO} mice) (Fig.4a). With the ability to trigger the loss of function in adult animals, we eliminate any developmental issues that could arise from a loss of *Paqr4*. After 2 weeks of dox-chow induction, gene rearrangements specifically occurred in adipose tissues, accompanied by a substantial decrease in *Paqr4* expression in Paqr4^{iAKO} mice (Extended Data Fig.5a–b).

Under dox-chow-fed conditions, Paqr4^{iAKO} mice displayed a subtle phenotype, with normal body weight, body composition, fat pad weights, and slightly decreased liver weights (Extended Data Fig.5c–e). There was no marked impact on glucose tolerance or insulin sensitivity, even after 8–9 weeks of dox-chow feeding (Extended Data Fig.5f–g), however, these parameters were slightly improved in older Paqr4^{iAKO} mice after 19–20 weeks of induction (Extended Data Fig.5h–j).

We examined the metabolic effects of PAQR4 loss in Paqr4^{iAKO} mice fed dox-HFD. Body weight gain was comparable after 18 weeks of dox-HFD feeding (Fig.4b–c). Paqr4^{iAKO} mice also displayed normal food intake and energy expenditure (EE) without appreciable effects on RER, VO_2, VCO_2, or physical activity (Extended Data Fig.5k–p). Furthermore, Paqr4^{iAKO} and control mice had comparable body composition and WAT mass (Fig.4d; Extended Data Fig.5q–r). However, the liver weight was reduced with diminished steatosis (Fig.4d–f; Extended Data Fig.5r). In addition, BAT mass was decreased with reduced lipid-droplet size and enhanced *Ucp1* expression (Fig.4d–e; 4g). Meanwhile, histological improvements were observed in WAT, accompanied by the downregulation of several inflammatory and fibrotic genes (Fig.4e; 4h–i). Circulating leptin levels were decreased, whereas adiponectin levels were increased (Fig.4j–k), suggesting improved adipose function without any impact on overall fat mass. Moreover, Paqr4^{iAKO} mice exhibited moderately improved glucose tolerance and insulin tolerance after 2 weeks of dox-HFD feeding (Extended Data Fig.5s–u). Importantly, under more severe conditions, 19–20 weeks of dox-HFD feeding, Paqr4^{iAKO} mice displayed profound improvements in glucose tolerance and insulin-mediated glucose disposal (Fig.4l–n), along with enhanced insulin signaling (Supplementary Fig.1). In addition, we observed comparable improvements in glucose homeostasis with unaltered body weight upon deleting *Paqr4* in mice with pre-existing obesity (Fig.4o–q). Thus, in the absence of *Paqr4* in adipocytes, systemic metabolic homeostasis improves in the obese state.

PAQR4 promotes adipose remodeling and adipocyte de-differentiation

Having demonstrated that PAQR4 is a critical regulator in adipose tissue remodeling and thus systemic glucose homeostasis, we set out to determine the mechanistic basis of this connection. We first examined the role of PAQR4 on adipogenesis. Even though *Paqr4* is upregulated during adipocyte differentiation, its overexpression robustly downregulated mature adipocyte markers and inhibited adipogenesis *in vitro* (Extended Data Fig.6a). In contrast, deletion of *Paqr4* elevated the expression of adipogenic markers *Pparg2, Plin1* and *Adipoq* during early adipogenesis (Extended Data Fig.6b). However, PAQR4 exerted little effects on cell cycle during adipogenesis (Extended Data Fig.6c). To test the impact of PAQR4 on adipogenesis *in vivo*, we fed Paqr4^{ad} mice from embryonic stage (E13) with dox-chow and assessed adipose development. Interestingly, massive impairment was observed on postnatal day 7 (P7) in Paqr4^{ad}-gWAT which develops postnatally (Extended Data Fig.6d). Moreover, similar defects were also seen in sWAT and BAT which develop during earlier embryonic stages, with a more pronounced impairment on P7 (Extended Data Fig.6d–f). In Paqr4^{ad}-sWAT, prominent macrophage infiltration was observed on P7 (Extended Data Fig.6e). Accordingly, the size of sWAT and BAT was reduced on day P7 (Extended Data Fig.6g). At 6 weeks of age, Paqr4^{ad} mice displayed a 26% reduction in fat mass (Extended Data Fig.6h). Thus, PAQR4 exerts a negative role on adipogenesis both *in vitro* and *in vivo*.

We subsequently performed single-cell RNA sequencing (scRNA-seq) to access the remodeling of adipocyte progenitor pool (Fig.5a). We focused on the *Pdgfra*+ cells, as it's expressed visually in all adipose stem and progenitor cells (ASPCs) [27]. These cells also express canonical ASPC markers including *Pdgfrb*, *Ly6a* (*Sca1)*, *Cd34* and *Cd29*[27] (Fig.5b). Three subpopulations were identified which were resembling previously defined ASPC subpopulations according to the population-specific markers. P1 (*Dpp4*+ cells) and P2 (*Icam1*+) appeared to be represented 'ASC2' and 'ASC1' as defined by Burl *et al.* [28], or 'Group1' and 'Group2' defined by Merrick *et al.* [29], respectively (Supplementary Fig.2a–d). Whereas P3 was similar to 'Group3' from Merrick *et al.* [29], which expressed *F3* (encoding CD142), *Fmo2*, and *Gdf10* (Supplementary Fig. 2e). Schwalie *et al.*[30] defined an anti-adipogenic population of adipogenesis regulators (termed 'Aregs') which expressed *F3* and *Abcg1*. However, we did not detect *Abcg1* in the P3 (*F3*+) population (Supplementary Fig. 2e–f), in line with the mural-derived ASPCs (*Pdfgrb*+*Dpp4*−) which expressed *F3* but not *Abcg1* [31]. DPP4+ cells are considered as multipotent progenitors, whereas ICAM1+ and CD142+ cells are relatively restricted to the adipocyte lineage[29]. GO enrichment analyses further indicated altered pathways were related to inflammation and smooth muscle cell activation in all the subpopulations. However, steroid metabolic pathways were found to be altered only in P1 (*Dpp4*+ cells) (Fig.5c, Supplementary Fig.2g). Moreover, flow cytometry analysis indicated both ICAM1+ and CD142+ ASPCs were decreased by PAQR4, suggesting reduced adipogenic potential in the Paqr4^{ad} mice (Fig.5d; Supplementary Fig.3a). Thus, PAQR4 remodels the adipose stromal microenvironment into an environment less favorable towards adipogenesis.

Adipocyte turnover is tightly controlled under physiological conditions. As PAQR4 induction prompts a fat mass reduction in adult mice, we wondered what the impact

is on adipocyte turnover. To study this, we crossed Paqr4^{ad} mice to our "AdipoChaser" mice[4,32] (Adipoq-rtTA:TRE-Cre:Rosa26-mT/mG) (Fig.5e). This allowed us to examine the effects of PAQR4 on adipocyte fate via a "pulse-chase" labeling strategy. Following 2 weeks of dox induction, all adipocytes in control mice were efficiently labeled with EGFP (EGFP^{+}/Perilipin^{+}, Fig.5e). Interestingly, in contrast to control adipose tissue, a lot of EGFP^{+}/Perilipin^{-} fibroblast-like cells appeared in sWAT and, to a lesser extent, in gWAT of Paqr4^{ad} mice (Fig.5e, Supplementary Fig.3b). This reflects that these cells were in the fully developed mature adipocyte stage at induction during the labelling period, but subsequently lost their adipocyte identity and morphed into fibroblasts. Flow cytometry analysis further suggested that such de-differentiated adipocytes express the fibroblast marker PDGFRβ and can contribute up to ~9% of the stromal vascular pool of cells (Fig.5f). Interestingly, these de-differentiated adipocytes re-differentiated into mature adipocytes within 4 weeks of dox-withdrawal (Fig.5e, Supplementary Fig.3b), clearly reflecting that the process of PAQR4-induced de-differentiation is reversible. This suggests that we do not lose any cells due to necrosis or apoptosis upon PAQR4 induction. In fact, we were unable to observe any signs of adipocyte death (Supplementary Fig.3c). In light of this, we also tested whether the withdrawal of dox can reverse the metabolic deficiencies in Paqr4^{ad} mice. We first fed Paqr4^{ad} mice with dox-HFD for 6 weeks and then switched to HFD without dox. As expected, body weight gain increased shortly after dox-withdrawal. Subsequent re-exposure to dox rapidly reduced weight again (Fig. 5g–h). Moreover, hyperglycemia, hyperinsulinemia, and hypoleptinemia were largely recovered following dox removal (Fig.5i–k). Interestingly, dox withdrawal even improved glucose tolerance (Fig.5l), potentially reflecting enhanced leptin sensitivity after prolonged suppression of leptin, albeit this improvement eventually disappeared again (Fig.5m).

Blocking ceramide synthesis improves PAQR4-induced metabolic defects

PAQR4 displays a high sequence similarity with other class I PAQR family members, such as AdipoR1/2. Given the critical role of AdipoR1/2 in ceramide metabolism, we wondered whether PAQR4 is involved in the regulation of ceramide levels as well. PAQR4 indeed exhibited profound effects on sphingolipid metabolism. In contrast to the role of AdipoR1/2 that effectively lower ceramide levels, PAQR4 increased multiple ceramide species in gWAT and sWAT, with the most pronounced increases observed in very long-chain ceramides (C24:1 and C24:0) and more moderate increases in long-chain C16:0 ceramide (Fig.6a; Extended Data Fig.7a). Moreover, multiple species of dihydroceramides, hexosylceramides, sphingomyelin, and lactosylceramides were also elevated in Paqr4^{ad} adipose tissues. We also saw an increase in sphinganine, sphingosine, and sphingosine-1-phosphate in Paqr4^{ad}-gWAT and -sWAT (Extended Data Fig. 7b–c). This was also observed when these species were measured in serum, where ceramides, dihydroceramides, and hexosylceramides were significantly increased (Supplementary Fig.4a–b). Thus, PAQR4 appears to induce multiple lipids in the sphingolipid pathway (Fig.6b). In contrast, in Paqr4^{iAKO} mice, various components of the sphingolipid pathway were decreased, an effect that was more pronounced in gWAT than in sWAT (Fig.6a; Extended Data Fig.7a–c). As for ceramides, C16:0 and C18:0 ceramides were most significantly reduced in Paqr4^{iAKO}-gWAT and sWAT. However, compared to the changes in serum sphingolipids in Paqr4^{ad} mice, Paqr4^{iAKO} mice showed more moderate changes (Supplementary Fig.4a–b), suggesting

other tissues may compensate for the lack of PAQR4 in adipocytes in Paqr4^{iAKO} mice. Nevertheless, these gain- and loss-of-function findings suggest PAQR4 exerts profound effects on ceramide homeostasis.

Similar to our observations *in vivo*, PAQR4 increased ceramide species *in vitro* in adipocytes, perturbing sphingolipid metabolism (Supplementary Fig.5a–b). Deletion of *Paqr4* in adipocytes showed a more subtle impact on sphingolipid levels, indicating a compensatory mechanism for ceramide generation may present (Supplementary Fig.5a–b). *Adipor1* and *Adipor2* were downregulated by PAQR4, which may contribute to the ceramide accumulation due to the overall cellular reduction of ceramidase activities (Supplementary Fig.6a–b).

Ceramide overload may affect glycerolipid metabolism due to fatty acid availability. We thus examined glycerolipids including triacylglycerol (TG) and phospholipids (Supplementary Fig.7). Indeed, most of TG species were reduced with the exception of a few that were increased in both Paqr4^{ad}-gWAT and sWAT (Supplementary Fig.8a). In addition, multiple classes of glycerophospholipids and lysoglycerophospholipids were largely increased, except that, LPS and LPI were exclusively reduced in Paqr4^{ad}-sWAT (Supplementary Fig.8b; 9a–b). Interestingly, multiple polyunsaturated TGs were increased and saturated or monounsaturated TGs were reduced in Paqr4^{iAKO}-gWAT and sWAT (Supplementary Fig.10a). Another lipid classed altered by *Paqr4* deletion was phosphatidylserine (PS) with a number of species increased especially 38:6, 36:5, 36:4, 34:2 PS, both in gWAT and sWAT. However, other classes are largely unaltered (Supplementary Fig.10a–b; 11a–b). Thus, ceramide homeostasis is clearly closely associated with lipid metabolism in adipose tissues.

Ceramide signaling has a detrimental role on adipose function. We found that the presence of C2-ceramide (C2-Cer) potently inhibited adipogenesis *in vitro,* although we did not see an effect on the cell cycle (Extended Data Fig.6c; 8a). Moreover, exposing mature adipocytes to C2-Cer promoted the de-differentiation of mature adipocytes into ‘fibroblast’-like cells (Extended Data Fig.8b). In contrast, deletion of *Paqr4* diminished the inhibitory effects of C2-Cer on adipogenesis (Extended Data Fig.8c). Thus, PAQR4 impairs adipocyte function due to aberrant ceramide accumulation.

We therefore wondered whether blocking *de novo* ceramide biosynthesis could rescue the metabolic effects triggered by PAQR4 overexpression. We employed myriocin, a specific inhibitor of the rate-limiting ceramide synthesis enzyme SPT [9,33] (Fig.6b), in Paqr4^{ad} mice pre-exposed to 12 weeks of dox-HFD. In line with previous studies, myriocin reduced weight gain and improved systemic metabolism by enhancing liver and adipose tissue function in obese mice (Fig.6c–f; Extended Data Fig.8d–h). Myriocin also reduced food intake both in Paqr4^{ad} and control mice, but only during the early treatment (Extended Data Fig.8i). Interestingly, the inhibitor partially rescued the weight loss normally seen in the Paqr4^{ad} mice (Extended Data Fig.8d–e). Myriocin also improved adipose tissue health and reduced liver steatosis, albeit it did not affect fat pad weights (Fig.6c, Extended Data Fig.8g–h). It furthermore lowered hyperglycemia and hyperinsulinemia and improved glucose tolerance in Paqr4^{ad} mice (Fig.6d–f). In sWAT, gWAT, and adipocytes, ceramide

synthases 2 (CERS2) is the major isoform (producing C24 ceramides), followed by CERS5 (producing C16 ceramides) (Supplementary Fig.12a–b). We hence examined whether knockdown these *Cers* isoforms could mitigate adipose dysfunction in Paqr4^{ad} mice. Indeed, a local knockdown of the *Cers2* or *Cers5* in sWAT mediated adipocyte size and reduced adipose fibrosis, reflecting improvements in adipose tissue function, albeit it did not rescue weight gain or sWAT mass (Fig.6g–j, Supplementary Fig.12c–g). Nevertheless, it further improved glucose tolerance and insulin-mediated glucose disposal in Paqr4^{ad} mice (Fig.6k–l; Supplementary Fig.8h). Therefore, PAQR4-mediated changes in the sphingolipid pathway have a critical impact on adipose tissue metabolism. Blocking ceramide biosynthesis in the context of PAQR4 overactivation diminishes the negative effects of PAQR4 on adipose tissues.

PAQR4 regulates ceramide levels by mediating CERS activity

As AdipoR1/2 regulate ceramide metabolism through their ceramidase activities, we wondered whether PAQR4 also exhibits enzymatic activity. Strikingly, while we observed increases in ceramide levels by *Paqr4* overexpression (Fig.7a), PAQR4 itself did not show ceramide synthase (CERS) or ceramidase activities (Extended Data Fig.9a–c). We thus hypothesized that PAQR4 may act as an essential cofactor that promotes CERS activity. We hence examined whether co-expression of *Cers2* or *Cers5* together with *Paqr4* would further promote ceramide production. Indeed, *Paqr4* overexpression drastically elevated ceramide levels in cells co-expressing either *Cers2* or *Cers5* (Fig.7a). Moreover, PAQR4 potently enhanced CERS2 activity with C24:1 CoA as a substrate as judged by an increased production of C24:1 D7-dehydroceramide and the disappearance of D7-sphinganine (Fig.7b, 7d). PAQR4 also increased CERS5-induced consumption of D7-sphinganine, although no changes in C16:0 D7-dyhydroceramide levels were observed (Fig.7c–d). Notably, CERS2 activity was also enhanced by PAQR4 using C16:0 CoA as substrate, suggesting an indirect enhancement of activity (Fig.7b). Likewise, similar enhancement of CERS5 activity by PAQR4 was observed in the presence of C24:1 CoA (Fig.7c). Sphingolipids undergo degradation to provide sphingosine for ceramide synthesis through the salvage pathway. Increased CERS5-produced C16 ceramide upon PAQR4 co-expression might indirectly originate from this pathway, as CERS5 consumes much more sphingosine than CERS2 (Extended Data Fig.9d). Moreover, similar increases in ceramide production and enhancement of CERS2 activity were observed by *in vitro* combining lysates from cells individually overexpressing *Paqr4* or *Cers2*/*Cers5* (Extended Data Fig.9e–h). This further suggests that PAQR4 is a critical cofactor for CERS. Finally, we also observed enhanced CERS2 activity by PAQR4 overexpression when analyzing adipose tissue microsomes from Paqr4^{ad} mice (Fig.7e).

This raises the question as to the potential mechanism by which PAQR4 may enhance CERS activity. Gene expression levels of *Cers* were largely downregulated in adipocytes and Paqr4^{ad}-sWAT (Extended Data Fig.10a–b). However, CERS2 protein levels were increased in both sWAT and gWAT of Paqr4^{ad} mice (Extended Data Fig.10c). This increase was also observed in *Paqr4*-overexpressing cells (Fig.7f–g). CERS2 protein accumulated upon treatment with the lysosomal inhibitor bafilomycin A1 (BFA), but was not affected by the proteasome inhibitor MG132 (Fig.7f, Extended Data Fig.10d–e). This suggests that

CERS2 is predominantly subjected to lysosomal rather than proteasomal degradation. By using cycloheximide (CHX), or 'pulse chasing' with a CERS2-HaloTag, we determined that CERS2 has a relatively short half-life (~4 h), but its protein stability was enhanced by PAQR4 through inhibition of its lysosomal translocation and degradation (Fig.7f, 7h; Extended Data Fig.10f–g). Similarly, CERS5 protein also undergoes lysosomal degradation, but it has a relatively long half-life (>24 h), whilst its level was also increased by PAQR4 (Fig.7g; Extended Data Fig.10h–i). However, CERS5 protein levels eventually declined at 24 h post-treatment, possibly resulting from increased cellular toxicity due to accumulating C16 ceramide in presence of PAQR4 (Extended Data Fig.10h).

From unbiased proteomics, we found that PAQR4 interacted with CERS2 in adipocytes and HEK293T cells (Fig.7i; Supplementary Fig.13a). The interaction was confirmed by co-immunoprecipitations (Fig.7j; Supplementary Fig.13b) or NanoBiT proximity assays (Supplementary Fig.13c). Similar interactions of PAQR4 and CERS5 were also observed (Supplementary Fig.13a, 13c). Moreover, we found PAQR4 bound various ceramide species (Fig.7k–m). In addition, PAQR4 protein levels were decreased by ceramide but increased by myriocin treatment (Fig.7n; Supplementary Fig.13d). Myriocin further stabilized the PAQR4-CERS2/5 interactions, whereas these interactions were diminished by ceramide treatment (Fig.7o; Supplementary Fig.13e). Finally, in a classical Cleveland limited proteolysis assay, the presence of PAQR4 reduced the trypsin sensitivity of CERS2/5. In contrast, ceramide treatment enhanced trypsin sensitivity (Fig.7p; Supplementary Fig.13f–g), reflecting a conformational change stimulated by PAQR4 interacting with CERS. Thus, PAQR4 plays a critical role in ceramide homeostasis by mediating the stability and activity of CERS (Fig.7q).

Discussion

Adipose tissue remodeling is critical for maintaining normal adipose tissue function and systemic metabolic homeostasis. Our study also indicates that metabolic health can be influenced more significantly by the quality of adipose tissues rather than overall adiposity, a phenomenon also seen in *Ppara* or serine/threonine protein kinase 25 (*STK25*) deficient mice[34,35]. Many studies suggest that ceramide accumulation in multiple tissues, including adipose tissue, has considerable detrimental effects on local and systemic metabolism, and reducing ceramide levels in adipocytes has considerable beneficial effects[36]. Thus, targeting the sphingolipid pathway provides a promising strategy for multiple pathological conditions, including metabolic disorders and cancer[12,37]. Our study implicates PAQR4 as an important player in adipose tissue remodeling through its impact on ceramide metabolism. Moreover, manipulating ceramide levels by PAQR4 closely impacts adipose tissue health and systemic glucose control, highlighting PAQR4 as an attractive target in metabolic diseases.

Adipocyte cellularity is set at a young age, and maintained at a relatively constant number during obesity and weight loss in adulthood[38]. However, defects in adipogenesis are frequently associated with dyslipidemia and insulin resistance[39]. Modulating ceramide levels by PAQR4 exerts a profound impact on adipose remodeling, by both suppressing adipogenesis and triggering adipocyte de-differentiation. Our findings are in line with previous studies that ceramides robustly inhibit adipogenesis and impair adipocyte

function[9,40]. Moreover, adipocyte de-differentiation may be a major cause of metabolic defects in adulthood when *de novo* adipogenesis is limited, particularly in subcutaneous depots[41]. We believe that adipocyte de-differentiation contributes to the regulation of inflammation and fibrosis during adipose remodeling. Adipocyte de-differentiation is frequently seen in liposarcomas where it promotes inflammation and disease development[6]. Our recent observations suggest widespread de-differentiation of mammary adipocytes in proximity to tumor lesions[8]. These de-differentiated adipocytes morph into myofibroblasts and macrophage-like cells, exerting potent pro-mitogenic effects on surrounding breast cancer cells. Interestingly, adipocytes fail to maintain their cellular identity and exhibit myofibroblast-like features with mitochondrial deficits upon long-term HFD feeding in mice[42,43]. This “adipocyte to myofibroblast transition” (AMT) occurs and bestows adipose tissue fibrosis and inflammation under severe obese conditions[44]. However, the role of adipocyte de-differentiation is probably underestimated under these conditions due to the lack of specific markers to detect this phenomenon in human samples. The seemingly reversible nature of the de-differentiation events may contribute to the rebound in body fat that commonly occurs after weight loss. Yet, the exact molecular mechanisms underlying this unique plasticity of adipocytes remain largely unclear. Our findings suggest that increased ceramide levels are a main trigger of adipocyte de-differentiation in Paqr4^{ad} mice; however, further studies are needed to see how common a phenomenon this ceramide effect is in different settings. We further found that blocking ceramide biosynthesis can improve metabolic dysfunction not only in the obese state, but also under lipodystrophic conditions.

The adipocyte progenitor pool is critical for healthy adipose tissue remodeling under metabolic stressful conditions[31,45]. It is plausible that ceramides play a critical role for the cellular homeostasis of ASPCs and their functions. Our studies suggest that the activation of the PAQR4-ceramide axis disrupts the progenitor pool, and alters their transcriptional characteristics, likely contributing to the impairment of adipocyte turnover in the Paqr4^{ad} mice. ASPCs are highly responsive to metabolic challenges and are also involved in fibrogenesis and immunological functions[45]. For instance, overfeeding reduced the DPP4+ stem population and increased CD142 (*F3*+) fractions in visceral fat[29]. One specific visceral ASPC population referred to as ‘FIPs’ (fibro-inflammatory progenitors, PDGFRβ+LY6c+) was rapidly increased and further promoted adipose inflammation upon HFD-feeding[45]. In subcutaneous fat, both PDGFRβ+DPP4− and PDGFRβ+DPP4+ ASPC fractions are altered in response to hypoxia signaling in obesity, and contribute to adipose tissue fibrosis[31]. Our pathway analysis reflects inflammatory and fibrogenic features in the Paqr4^{ad}-ASPCs. It will be interesting to further examine the interactions between the de-differentiated adipocytes and the ASPCs. At this stage, it remains largely unknown how ceramide overload in adipocytes conveys signals to the progenitor cell pool.

Importantly, our findings suggest that the PAQR4-CERS axis serves as a feedback mechanism to maintain cellular ceramide levels. In this regard, PAQR4 may function as a ‘ceramide sensor’ by mediating CERS. However, more structural insights are needed to affirm this role of PAQR4. It is conceivable that the physical interaction of PAQR4 with CERS facilitates substrate accessibility of CERS, as PAQR4 alters their enzymatic activities, particularly for CERS2. PAQR4 does not show a preference for specific ceramide species. Rather, PAQR4 may depend on the cell type-specific expression pattern of *Cers* and the

cellular status. We found both CERS2 and CERS5, the major two isoforms in adipocytes, are regulated by PAQR4. Interestingly, CERS activity is regulated by dimerization between different isoforms, such as dimers of CERS2 and CERS5[46]. Thus, the interactions between the two CERS isoforms and PAQR4 may lead to alterations in different ceramide species from the salvage pathway. As such, we observed multiple ceramides are altered by PAQR4, although we did not see direct effects on CERS5 activity. Notably, manipulating only certain ceramide species rather than altering the entire ceramide profile may be sufficient to cause significant metabolic effects. For instance, *Cers6* deletion reduced C16 ceramides and protected against diet-induced obesity and liver steatosis[47], whereas mice with *Cers2* haploinsufficiency reduced C24-ceramides but increased C16-ceramides in the liver as a compensatory event and promoted liver steatohepatitis[48]. While we observe more robust changes in C24-ceramides in the Paqr4^{ad}-adipose tissues, we see a more selective reduction in C16 and C18-ceramides upon *Paqr4*-deletion. Therefore, the regulation of ceramide species may be dependent on the metabolic context.

Ceramide and glycerolipid homeostasis are closely associated[49]. We observed widespread changes for the glycerolipid composition by PAQR4 in adipose tissues. In Paqr4^{ad}-fat, the majority of the TG species were reduced. Excess fatty acids progress to ceramide synthesis when they fail to be incorporated into TG storage in adipocytes. Notably, *Paqr4*-deletion reduced saturated and monounsaturated TGs, but increased polyunsaturated TGs. This is in line with the notion that saturated but not unsaturated fatty acids are used for ceramide generation[50]. In addition, multiple species of glycerophospholipids and lyso-glycerophospholipids are altered by PAQR4, reflecting the tight connection between sphingolipid and glycerolipid metabolism. Many of these lipids are critical for membrane structure and signal transduction and are critically involved in the regulation of inflammation and insulin resistance[11,49]. However, the exact function of these lipids may be context-dependent, as many lipid species are regulated by PAQR4 in a distinct manner in different fat depots.

It is noteworthy that PAQR4 promotes tumorigenicity in multiple cancer types, including skin cancer, non-small cell lung cancer (NSCLC), prostate cancer, and breast cancer[51]. Moreover, *PAQR4* expression is negatively correlated with survival rate in patients with multiple cancer types[51]. Notably, ceramide metabolism has a profound effect on tumor growth and chemoresistance[37,52,53]. However, in cancer, the impact of ceramides may trigger dichotomous outcomes that likely depend on ceramide species and cellular responses[53]. While ceramides can induce apoptosis, increased ceramide levels and *CERS* expression can be found in different tumor types, and these can offer a distinct advantage for tumor progression[54–56]. Our findings reported here seem to be different from our previous study regarding the possible ‘ceramidase’ activity of PAQR4 which lowered ceramide levels in the context of tumor cells[18]. This difference may be attributed to the distinct cellular conditions, especially considering the substantial differences between highly proliferative and metabolically distinct cancer cells versus adipocytes. For instance, knockdown of PAQR4 elicited remarkable cell apoptosis in cancer cells but not in adipocytes[18]. However, ceramidases are substrate driven and can also exert the reverse activity to generate ceramides. This is dependent on the overall cellular context as well as the enzymatic microenvironment, such as substrate availability, pH values, and iron levels[57–59]. Future

efforts will have to determine the exact mechanism underlying the potential directional enzymatic activity of PAQR4.

Our studies have certain limitations. First, although we used inducible systems to mitigate possible developmental compensations, manipulations of gene expression levels in mice via overexpression or deletion may not accurately reflect its normal function in the native context. Second, our findings suggest PAQR4 regulates ceramide levels by influencing the stability of CERS, generic alterations in sphingolipids and glycerolipids in membranes may also affect the half-life of CERS; and the interactions of PAQR4 and CERS were determined using overexpression systems. Additionally, our proteomics data does not rule out other potential interactors with PAQR4 that may also contribute to its effects in adipocytes. Nevertheless, our findings unambiguously demonstrate that the activation of PAQR4 in adipocytes induces metabolic dysfunction.

Given PAQR4's involvement in mitogenesis in tumor cells, targeting PAQR4 is likely to benefit patients with metabolic diseases and different types of cancer, and it may be particularly powerful in the context of obese cancer patients.

Methods

Mouse Models

All mice used for experiments were on a pure C57BL/6J background. All mouse protocols were approved by the Institutional Animal Care and Use Committee of the University of Texas Southwestern Medical Center (APN: 2015–101207G). The following mouse lines were used.

- TRE-Paqr4
- Paqr4-flox
- Adipoq-rtTA
- TRE-Cre
- *ob*/*ob*
- Flp (neomycin) deleter
- Rosa26-mT/mG

TRE-Cre (stock# 006234), Lep^{ob} (*ob/ob*, stock# 000632), Flp (neomycin) deleter (stock# 007844) and Rosa26-mT/mG mice (stock# 007676) were obtained from The Jackson Laboratory. Adipoq-rtTA [60,61] and TRE-Paqr4 mouse lines were generated in house. Paqr4-flox mouse line was generated by Shanghai Model Organisms (www.modelorg.com) in collaboration with the Helmholtz Zentrum München. The details for both constructs are below:

The gene encoding mouse PAQR4, *Paqr4*, is located on Chromosome 17 and features 3 exons. The construct used to generate Paqr4-transgenic and flox mice was based on the sequence of the mouse *Paqr4* gene (Ensembl: ENSMUSG00000023909). To generate TRE-

Paqr4 mice, the full length *Paqr4*-coding sequence was subcloned into the TRE vector[60,61] with a rabbit β-globin 3'-UTR. The construct was injected into fertilized (C57BL/6N) F1 mouse eggs at the UT Southwestern Medical Center Transgenic Core. The resulting transgenic mice were bred to C57BL/6J mice. Founders were screened for expression and specificity by crossing TRE-Paqr4 mice with Adipoq-rtTA mice (referred to as the Paqr4^{ad} mice) to ensure specific and inducible expression in adipocytes.

To generate Paqr4-flox mice, a LoxP site was inserted in exon 3. A phosphoglycerine kinase (PGK)/Neo cassette flanked by FLP recombinase target (FRT) and another LoxP site was inserted between exons 1 and 2. These mice were first crossed with Flp deleter mice to excise the PGK/Neo cassette to generate Paqr4$^{floxed/floxed}$ mice. Homozygous Paqr4$^{floxed/floxed}$ mice were then crossed with TRE-Cre and Adipo-rtTA mice to obtain inducible and adipocyte-specific iAKO (Paqr4$^{floxed/floxed}$:TRE-Cre:Adipoq-rtTA) mice, which were verified by PCR with adipose tissue specific *Paqr4* recombination and mRNA levels.

AdipoChaser (TRE-Cre:Adipoq-rtTA:Rosa26-mT/mG) mice were generated as previous reported[4]. Paqr4Chaser (TRE-Cre: TRE-Paqr4: Adipoq-rtTA: Rosa26-mT/mG) mice were generated by crossing TRE-Paqr4 mice with AdipoChaser mice.

ob/*ob*:Paqr4^{ad} mice were generated by crossing *Ob/ob* (heterozygous) mice with Paqr4^{ad} mice. Offspring inheriting both heterozygous *ob* mutant and TRE-Paqr4 genes were crossed back with *Ob*/*ob* mice to obtain *ob*/*ob*:Paqr4^{ad} (*ob*/*ob*:TRE-Paqr4:Adipoq-rtTA) mice. *Ob*/*ob* mice were used as controls.

Mouse Studies

Mice were housed at 22°C, 45% humidity with 12-hour light-dark cycles and free access to water and food unless otherwise indicated. Standard chow (Lab Diet, #5058), 60% high-fat diet (HFD) paste (#S3282, BioServ), doxycycline (dox)-containing chow (#S4107, BioServ) or dox-containing HFD paste (#S7067, BioServ) (600 mg/kg unless otherwise indicated), were provided for the indicated time periods. In the dox-does response studies, HFD paste containing 0, 50, 100, 200, and 600 mg/kg of dox were applied. Male mice and their littermate controls were used as female mice are more resistant to develop obesity and type 2 diabetes. Adipo1-rtTA mice were used as controls for Paqr4^{ad} mice; Adipoq-rtTA X Paqr4$^{floxed/floxed}$ were used as controls for Paqr4^{iAKO} mice. Experiments were started with mice at eight weeks of age except for the *in vivo* adipogenic studies. To access *in vivo* adipogenesis, mice were fed with dox-chow at adipose developmental stage on embryonic day 13 (E13) [32]. Adipose tissues were harvested at E18, postnatal day 1 (P1) and 7 (P7) for histological analyses.

Adipocyte Lineage Tracing

Paqr4 Chaser mice and their littermate controls were fed dox-chow for 2 weeks to label adipocytes. For adipocyte recovery, mice were switched to a standard chow (lacking dox) for 4 weeks. Adipose tissues were harvested for histological analyses.

Pharmacological Treatments

To avoid the effects of obesity-associated leptin resistance, *in vivo* leptin treatment was performed with chow-fed mice. Paqr4^{ad} and control mice were first fed dox-chow for 14 weeks and then treated with recombinant mouse leptin (~5 μg/day/mouse, Lot# AFP1819, National Hormone & Peptide) via an ALZET osmotic minipump (Model 1002, DURECT Corporation) for another 2 weeks.

For myriocin treatment, Paqr4^{ad} and control mice were first fed dox-HFD for 12 weeks and then switched to myriocin containing dox-HFD (0.5 mg/kg, cat# M1177, Sigma) for another 5 weeks.

For insulin-stimulated Akt signaling studies, mice were anesthetized, and a portion of the tissues was harvested (for basal conditions). Surgical threads were applied to prevent bleeding. Mice then received insulin (1 U/kg body weight) via retro-orbital injections. After 10 min, tissues of interest were quickly removed (insulin-stimulated condition) and frozen in liquid nitrogen and then −80 °C. Tissue lysates were prepared, and Akt signaling was examined by immunoblotting, as described below.

Biochemical Analyses

Serum insulin, leptin, and adiponectin were determined by commercially available ELISA kits (for insulin, cat# 80-INSMS-E10, ALPCO; for leptin, cat# 90030, CrystalChem; for adiponectin, cat# EZMADP-60K, EMD Millipore) following the manufacturers' instructions. Alternatively, serum adiponectin levels were determined by Western blotting as described below. Serum alanine transaminase (ALT) was measured using a commercial kit (cat# 700260, Cayman Chemical).

Body Composition Analyses

Fat mass and lean mass of chow-fed and HFD-fed mice were measured using a Bruker Minispec mq10 system (Bruker).

Computerized Tomography (CT) imaging

Mice CT imaging was performed with Mediso NanoScan (Budapest, Hungary). In brief, mice were anesthetized using 3% isoflurane and then placed onto the imaging bed under 2% isoflurane during the scanning. CT images were acquired with the following parameters: X-ray power 70 kVp and 800 μA, exposure 300ms, and a binning factor of 1:4. Regions of interest (ROI) were selected and fad pad volume was measured by using VivoQuant workstation (Invicro).

Cold Tolerance Test

Body temperature was measured by Transponder and Reader Systems (BMDS). In brief, mice were implanted with a transponder (IPTT-300) on the back and allowed to recover for one week. An acute cold challenge was performed by placing the mice in a temperature-controlled room (5°C) in the absence of food. Body temperature was measured at the indicated time points with the IPTT Reader. After the acute test, mice were refed and

acclimated to 5°C ambient temperature for 3 weeks. Afterwards, food was removed and body temperature was measured again at the indicated time points.

Adeno-associated Virus (AAV) Based Knockdown

Two separated CRISPR guide RNAs targeted for mouse *Cers2* (g1: GCCTCTGATGTCAAGCGAAAG; g2: GCCAGGGGTGTTGCCACATAA) and *Cers5* (g1: CAATGCTGGTTTCGCCATCGG; g2: GGAATCAGATTTCTCTGGTCG), and control *LacZ* (CTTCATACTGCACCGGGCGGG) were cloned into pX601 (Addgene#61591). AAVs (serotype of AAV2/Rec2) were produced, and the titers were determined as described previously[62]. Mice were fed HFD (without dox) for two weeks, and then AAVs (mix of the two gRNAs) were injected locally in both sites of inguinal fat pads ($5X10^{11}$ genome copies per site). After another two weeks, mice were switched to dox-HFD for the indicated time periods. The knockdown of *Cers2* was confirmed at the protein level in mouse AML12 cells but not in sWAT, and *Cers5* was not confirmed by Western blotting due to the lack of a viable antibody that works in tissue lysates. However, these specific guide RNAs targeting Cers2/5 successfully ameliorated adipose dysfunction in the $Paqr4^{ad}$ mice, indicating an effective gene knockdown.

Metabolic Cage Studies

The metabolic cage studies were performed by the University of Texas Southwestern Medical Center Metabolic Phenotyping Core facility as previously described [61]. Briefly, mice were acclimated with single housing for one week and then metabolic parameters including oxygen consumption (VO_2), CO_2 generation, food intake, and physical activities were monitored and recorded using a TSE Calorimetric System. Under fasting conditions, mice were fasted at night (~6 pm) and refed the next day (~6 pm). Mice had free access to water during the whole experiment. Respiratory exchange ratio (RER), energy expenditure (EE), and carbohydrate/fat oxidation were calculated as previously described[63].

Adipose Transplantation

$Paqr4^{ad}$ and control mice were fed dox-chow for 10 weeks and then received sWAT from three 4-week-old male C57BL/6J donor mice as previously described [64]. Briefly, recipient mice were anesthetized with 2–5% (v/v) isoflurane vapor with 95% O_2 (v/v) during the surgery. Donor fat pads were quickly isolated and immediately loaded to the corresponding subcutaneous site with a 16-gauge syringe. The process was performed within 10 min to minimize the ischemia time. Mice were maintained on dox-chow after the transplantation.

Systemic Metabolic Tests

Oral glucose tolerance tests (OGTTs) and insulin tolerance test (ITTs) were performed following standard protocols [63]. Briefly, mice were fasted for 6 h before administration of glucose (2g/kg body weight by gastric gavage) or insulin (0.5 U/kg for chow-diet and 0.75 U/kg body weight for HFD-fed mice by i.p. injection). During the tests, blood glucose levels were monitored with a glucose meter at the indicated time points. In addition, blood samples were collected during OGTTs from tail vein during the tests. Serum levels of insulin were determined as described below.

Histology and Immunostaining

Mouse tissues were dissected and fixed in 10% formalin overnight. Paraffin processing, embedding, sectioning, and hematoxylin/eosin staining as well as trichrome staining were performed by John Sheldon at UTSW Medical Center. Adipocyte size and fibrosis including extracellular matrix thickness, fibrous area and fibrous fraction were analyzed by Image J as previously described [8]. Immunostaining was performed following standard protocols with the following primary antibodies: Perilipin (1:700, cat# 20R-PP004, Fitzgerald), EGFP (1:500, cat# ab13970, Abcam), Mac2 (1:750, cat# CL8942AP, CEDARLANE), S100A4 (1:200, cat# ab41532, Abcam), KDEL (1:200, cat# ab176333, Abcam), LASS2/CERS2 (1:200, Santa Cruz, cat# sc-390745), Insulin (1:500, cat# A0564, Dako), and Glucagon (1:500, cat# ab92517, Abcam), and secondary antibodies (all 1:400 dilution), respectively: goat anti-guinea pig IgG (H+L) Alexa Fluor™ 594 (Invitrogen, cat# A11076), goat anti-chicken IgY (H+L) Alexa Fluor™ 488 (Invitrogen, cat# A11039), donkey anti-rat IgG (H+L) Alexa Fluor™ 488(Invitrogen, cat# A21208), goat anti-rabbit IgG (H+L) Alexa Fluor™ Plus 488 (Invitrogen, cat# A32731), chicken anti-mouse IgG (H+L) Alexa Fluor™ 594 (Invitrogen, cat# A21201), goat anti-guinea pig IgG (H+L) Alexa Fluor™ 488 (Invitrogen, cat# A-11073), donkey anti-rabbit IgG (H+L) Alexa Fluor™ 594 (Invitrogen, cat# A-21207). To determine apoptosis, TUNEL staining was performed with a commercial kit (cat# C10617, Invitrogen). Samples treated with DNase I were used as positive controls. Images were acquired on an Olympus FSX100 Microscope or LSM510 confocal microscope (Zeiss) and analyzed with Image J software. Representative of 3–7 biological replicates for histological analyses were shown.

Lipidomics studies

Ceramides and other sphingolipids were quantified by liquid chromatography-electrospray ionization–tandem mass spectrometry using a Nexera ultra-high-performance liquid chromatograph coupled to an LCMS-8050 (Shimadzu Scientific Instruments, Columbia, MD) as previously described [65]. Data are provided as pg/mg tissue for tissue samples, pg/ml for serum samples, and pg/μg protein for cellular samples.

For triacylglycerol profiling, an equivalent to 500 μg of adipose tissue lipid extract containing 20 μL of SPLASH LIPIDOMIX Mass Spec Standard (diluted 1:10 in MeOH, Avanti Polar Lipids, Alabaster, AL) were reconstituted in 225 μL of organic solvent mixture (CH_2Cl_2:MeOH 25:200, v:v). 0.3 μL of final extract was injected onto a Nexera LC-40 UHPLC system coupled to a Shimadzu LCMS-9030 Q-TOF mass spectrometer (Shimadzu Scientific Instruments). Triacylglycerol species were resolved on a reverse-phase C18 column as described by Rampler *et al.* [66] Triacylglycerols were identified as ammoniated adducts in positive ion mode (Putative identification of m/z at 5 ppm tolerance via cross-referencing with the LIPID MAPS database. The LIPID MAPS® Lipidomics Gateway, https://www.lipidmaps.org/). For phospholipids profiling samples containing an equivalent to 10 mg of adipose tissue lipid extract were analyzed as previously described [62]. For triacylglycerols and phospholipids, relative abundance was presented.

Fluorescent Enzymatic Assay

Ceramide synthase assays were performed as previously described [67]. Briefly, HEK293T cells were transfected with pCMV-3xFLAG-Paqr4 or empty vector for 48 h. Cell lysates were prepared in a buffer containing 20 mM HEPES (pH 7.4), 25 mM KCl, 2 mM $MgCl_2$, 250 mM sucrose, and protease 1X inhibitor cocktail (Thermo Fisher Scientific). 50 μg lysate were used in the assay in a reaction buffer containing 20 mM HEPES (pH 7.4), 25 mM KCl, 2 mM $MgCl_2$, 0.5 mM DTT, 0.1% (w/v) fatty acid-free BSA, 10 μM NBD-sphinganine (Avanti), and 50 μM fatty acid-CoA (Avanti). The reactions were conducted at 35°C for 30 min and lipids were extracted with chloroform: methanol (2:1). Samples were resolved in chloroform: methanol: H_2O (8:1:0.1, v/v/v) with aluminum-backed Silica Gel 60 TLC plates (Millipore). Alkaline ceramidase assays were examined as previously described [68]. Briefly, 100 μg lysate were used in the assay in a buffer containing 25 mM Tris-HCl buffer (pH 8.5) and 5 μM NBD-C12 ceramide (Cayman). The reactions were carried out at 37°C for 16 h. Lipids were then extracted with chloroform: methanol (2:1) and resolved in TLC plate as above with a developing buffer containing chloroform: methanol: 25% ammonia (90:20:0.5, v/v/v). Fluorescence-labeled products in the plate were detected with ChemiDoc MP Imaging System (Bio-Rad).

LC-MS/MS Based CERS Enzymatic Assay

As CERS2 and CERS5 are the major isoforms of ceramide synthases in adipocytes, which mainly produce C24 and C16 ceramides, respectively, we examined the effect of PAQR4 on the enzymatic activities of CERS2 and CERS5. Briefly, HEK293T cells were co-transfected with pRB-Myc-Cers2 or pRB-Myc-Cers5 along with pCMV-3xFLAG-Paqr4 or control empty vector for 48 h. Cell lysates were prepared and used in the enzymatic assay as aforementioned. In the assays with combined lysates, individual lysates overexpressed CERS2 or CERS5 were combined with PAQR4-expressed lysates for 30 min on ice, respectively, and then the enzymatic assay was performed as aforementioned. To measure the effect of PAQR4 on ceramide synthase activity *in vivo*, adipose tissue microsomes isolated from $Paqr4^{ad}$ and WT control mice were used. Briefly, mice were fed with dox-chow for 2 weeks and gWAT and sWAT were dissected. Samples from 3 mice were pooled together and homogenized in the lysis buffer mentioned above by using a Dounce homogenizer. Samples were then centrifuged at 680 g for 15 min and the fat-free extract was collected, followed by centrifugation at 10,000 g for 20 min. The clear, post-mitochondrial supernatant fraction was collected and further centrifuged at 105,000 g for 1 h. The final pellet which provided the microsomal fraction was resuspended in the lysis buffer and used for the activity assay. 25 μg microsomal protein were used in each reaction.

Ceramide formation with the cell lysates and adipose tissue microsomes were determined using LC-MS/MS. The assay was conducted essentially as the fluorescent assay described above except that NBD-sphinganine was replaced with stable isotope labeled D7-sphinganine (Avanti). C24:1 CoA and C16:0 CoA were used as substrates for accessing CERS2 and CERS5's activity, respectively. Products of C24:1 and C16:0 D7-dehydroceamide (D7-DhCer) that are generated from the substrates D7-sphinganine and C24:1 or C16:0 acyl-CoA, which are mainly utilized by CERS2 and CERS5, respectively, reflecting their enzymatic activities. Peak area of metabolite vs internal standard was

calculated. Internal standards were all added at 0.25 μM. The area ratios directly correlate with concentrations and were used to present the data as relative abundance.

Stromal Vascular Cells and Adipocyte Differentiation

Paqr4^{ad} and iAKO mice and their respective littermate control mice were used. Stromal vascular fraction (SVF) cells were isolated from sWAT as previously described [63]. To induce adipogenesis, confluent SVF cells were switched to adipogenic induction medium contained 5 μg/ml insulin, 1 μM dexamethasone, 500 μM isobutylmethylxanthine (IBMX), and 0.5 μM rosiglitazone. Cells were supplied with maintenance media containing 5 μg/ml insulin 2 days after induction. To test the effect of PAQR4 on adipogenesis, dox (2.5 μg/ml) was added to the adipogenic induction medium to induce *Paqr4* expression or deletion and maintained at the same dose during differentiation process. C2-ceramide (5 μM, cat# sc-201375, Santa Cruz) was added from the beginning of differentiation to examine its effect on adipogenesis. To induced de-differentiation, SVF cells were first differentiated into mature adipocytes and C2-ceramide (5 μM) was added from day 8 post-differentiation. Adipogenesis was assessed by Oil Red O staining as previously described [69].

Flow Cytometry

Subcutaneous adipose tissues (sWAT) from two mice were pooled for each sample. To examine adipocyte de-differentiation, SVF cells were isolated from Paqr4Chaser and Adipochaser control mice fed with dox-chow for 2 weeks. Red blood cells in the SVF pellets were lysed with RBC lysis buffer (Sigma). For blocking, cells were incubated in 2% FBS/PBS blocking buffer containing anti-mouse CD16/CD32 Fc Block (1:200) for 15 min on ice. Cells were stained with anti-mouse antibodies against BV421-CD31 (cat# 102423, BioLegend), BV421-CD45 (cat# 103133, BioLegend), and APC-PDGFRβ (cat# 136007, BioLegend) at 1:100 dilution for 30 min on ice in dark. After the incubation, cells were washed twice with 2% FBS/PBS and analyzed using a BD Biosciences LSR II cytometer (UTSW Flow Cytometry Core Facility). To quantify the adipose stem and progenitor cells (ASPCs), SVF cells were stained and analyzed as above using the following antibodies: PE/Cy7-CD31 (cat# 102418, BioLegend, 1:600), PE/Cy7-CD45 (cat# 103114, BioLegend, 1:600), PE/Cy7-TER119 (cat# 116222, BioLegend, 1:600), FITC-CD26/DPP4 (cat# 137806, BioLegend, 1:200), PE-CD54/ICAM1 (cat# 116108, BioLegend, 1:100), BV711-SCA1/LY6a (cat# 108131, BioLegend, 1:600), and APC-CD142/F3 (cat# 50413-R001, SinoBiological, 1:100) as previously described [29]. CD142 was preconjugated with APC using APC Conjugation Kit - Lightning-Link® (cat# ab201807, Abcam). Live single cells were first gated for ASPCs with Lin-(CD31−/CD45−/TER119−) SCA1+, and then gated for CD142+ and CD142− populations. CD142− population was further gated for ICAM1+ and DPP4+ subpopulations. Flow cytometry plots were generated using FlowJo (V10.8.1).

Single-cell RNA Sequencing (scRNA-seq)

Paqr4^{ad} and littermate control mice at eight weeks of age were fed with dox-HFD for two weeks. Inguinal adipose tissues were dissected and pulled together from three mice for each group. SVF cells were isolated, stained with anti-CD45-BV421 antibody (cat#103133, BioLegend,) to exclude leukocytes. CD45− cells were sorted by flow

cytometry (BD Biosciences FACSAria) and used for scRNA-seq. Sample preparation and library construction were performed following standard procedures provided from 10X Genomics Chromium as described previously [8]. Sequencing was conducted on Illumina NovaSeq 6000 system by Novogene (Sacramento, CA), yielding ~ 220 million reads per sample. Data pre-processing was conducted with Cell Ranger (v7.0.0) with default parameters, including sample demultiplexing, alignment, UMI (unique molecular identifier) collapsing, counting and initial quality control. Seurat R package (v4.1.1; Satija Lab, Seurat; https://satijalab.org/seurat/) was further used for data quality control and data visualizing in RStudio (v2023.06.2+561). Briefly, cells with very few genes (< 200), genes with non-zero counts in at most 3 cells, or unexpected very high feature counts (> 8000) were filtered out. Majority cells were *Pdgfra*+, a canonical marker for ASPCs. These cells (1368 cells from Paqr4^{ad} and 1173 cells from control data) were aggregated for single cell transcriptional comparisons. ASPCs were clustered into three subpopulations based on the upregulated signature genes and consensus knowledge of canonical gene markers of adipose stem cells. Gene ontology (GO) enrichment analyses were conducted between control and Paqr4^{ad} samples for each subpopulations with DAVID 2021 (https://david.ncifcrf.gov/).

Cell Cycle Analysis

Upon starting adipocyte differentiation, SVF cells were infected with AAVs (pAAVK CAG-[3x] FLAG-Paqr4 or pAAVK CAG-eGFP, MOI 10, 000 genome copies/cell) in the presence of vehicle or C2-ceramide (5 μM) for two days. Cells were harvested and fixed in ice-cold 70% ethanol, and then cells were treated with 100 μg/ml ribonuclease for 5 min at room temperature. After staining with propidium iodide (50μg/ml), the cell cycle stage was analyzed by flow cytometry.

Assessment of Protein Degradation

To determine the effect of PAQR4 on the protein stability of CERS2 and CERS5, HEK293T cells were co-transfected with pRB-Myc-Cers2 or pRB-Myc-Cers5 along with pCMV-3xFLAG-Paqr4 or control empty vector for 40 h, and then treated with 100 μg/ml cycloheximide, 10 μM MG132, or 1 μM Bafilomycin A1 (Sigma), respectively, for the indicated time points. Alternatively, HEK293A cells transfected with pcDNA3.1 (+)-Cers2-Halo or pcDNA3.1 (+)-Cers2-Halo, with pcDNA3.1 (+)-SNAP-Paqr4 or control vectors for 24 h. Cell were then treated with 1 μM Bafilomycin A1 for 8 h. CERS2 or CERS5 was labeled with HaloTag TMR ligand (cat# G8251, Promega) and PAQR4 was labeled with SNAP-Cell Oregon Green (cat#S9104, New England BioLabs). Cells were then fixed and stained with anti-LAMP1 antibody (1:200, Cell Signaling, cat# 9091). Images were acquired using confocal microscope. For ‘pulse tracing’ studies, CERS2 and PAQR4 were first labeled as described above, and images were taken at the indicated time points. Florescent density was measured by Image J software.

Protein - protein Interaction Studies

Unbiased proteomics was performed to identify potential PAQR4 interactors. For differentiated adipocytes, cells were infected with AAVs (pAAVK CAG-[3x] FLAG-Paqr4 or pAAVK CAG-eGFP, MOI 10,000 genome copies/cell) for two days. For HEK293T, cells were transfected with pCMV-3xFLAG-Paqr4 or a control empty vector for two days. Cell

lysates were immunoprecipitated with anti-FLAG M2 magnetic beads (Sigma, cat# M8823), followed by SDS-PAGE, and analyzed by mass spectrometry. Data were processed with the Perseus software platform (v2.0.11) (https://maxquant.net/perseus/), with fold change >2, FDR <0.01. Undetermined values were imputed with sample minimum.

To examine the interaction of PAQR4 and ceramide synthases, cells overexpressing Myc-CERS2 or Myc-CERS5 combined with FLAG-PAQR4 for 24 h were treated with 10 μM myriocin or 5 μM C2-Ceramide for another 24 h. Cell lysates were immunoprecipitated with mouse anti-FLAG M2 magnetic beads, Western blotted, and analyzed with rabbit anti-Myc antibody. The binding of FLAG-PAQR4 and endogenous CERS2 was examined both in adipocytes and HEK293T cells. After immunoprecipitation, samples were subjected to immunoblotting and detected by rabbit anti-CERS2 antibodies as described below. The interaction of ceramides with FALG-PAQR4 and CERS2 was tested using anti-ceramide IgM (Enzo Life Sciences, cat# ALX-804–196-T050) for immunoprecipitation, and further detected with anti-FLAG and CERS2 antibodies, respectively.

For NanoBiT protein: protein interaction, HEK293A cells were transfected with pcDNA3.1(+)-N-SmBit-Paqr4 together with pcDNA3.1(+)-Cers2-C-LgBit or pcDNA3.1(+)-Cers2-C-LgBit overnight. Luminescence was detected using the Nano-Glo® Live Cell Assay System (Promega). Co-transfection of FRB-LgBiT and FKBP-SmBiT vector was severed as positive control, with the stimulation of rapamycin (30 nM).

Trypsin Sensitivity Assay

Trypsin sensitivity assay was performed as previously described [70]. Briefly, HEK293T cells were co-transfected with pRB-Myc-Cers2 or pRB-Myc-Cers5 along with pCMV-3xFLAG-Paqr4 or control empty vector for 24h, and then cells were treated with C2-ceramide (5 μM) overnight. Lysates were prepared with lysis buffer containing 50mM Tris/HCl (PH8.0), 150 mM NaCl, 1% NP-40, 2 μM Z-VAD-fmk, 20 μM MG132 and 5 μM bafilomycin A1. Trypsin digestion was performed at various doses as indicated at room temperature for 15 min. The reactions were terminated by adding 2X SDS sample buffer containing 100 mM dithiothreitol and 8 mM PMSF. Samples were boiled for 5 min and subjected to SDS-PAGE and immunoblotting. For the assays with combined lysates, individual PAQR4 or CERS2/5 overexpressed lysates were first combined and treated with C24:1 and C16:0 ceramides (50 μM) for 45 min before trypsin digestion.

Lipid Overlay Assay

Lipid overlay assay was performed as previously described [71]. Briefly, a panel of natural ceramides (Cayman) were spotted on PVDF membranes, range from 0.5 – 2 nmol, and let it dry at room temperature for 60 min. Membranes were then blocked with 3% BSA in PBS containing 0.1% Tween 20 (v/v). Adipocyte lysates with FLAG-Paqr4 overexpressed were added and incubated at 4 °C overnight. Bound PAQR4 was detected with rabbit anti-FLAG antibody.

Western Blotting

Tissues and cells were lysed and protein concentrations were determined using the BCA method. Tissue or cell lysates (10 μg/lane) or serum samples (0.5 μl/lane) were boiled at 95°C in a protein loading buffer and separated on 4–12% sodium dodecyl sulfate-polyacrylamide gels (Bio-Rad). Antibodies against mouse adiponectin (1:1000, homemade), phospho-Akt (Ser473) (1:1000, cat# 4060, Cell Signaling), Akt (pan) (1:1000, cat# 2920, Cell Signaling), Myc-tag (1:1000, cat# 2278T, Cell Signaling), FLAG-tag (1:1000, cat# 14793, Cell Signaling), CERS2 (1:1000, cat# HPA027262, Sigma), and β-tubulin (1:1000, cat# 86298, Cell Signaling) followed by the respective fluorescence-conjugated secondary antibodies (1: 10000 dilution, IRDye, LI-COR, Lincoln, NE, USA): 800CW goat anti-rabbit IgG (cat# 926–32211), 680RD donkey anti-mouse IgG (cat# 926–68072), 800CW goat anti-mouse IgG (cat# 926–32210), or 680RD goat anti-rabbit IgG (cat# 926–68071) were used. Images were acquired and the fluorescent density was quantified by utilizing a LI-COR Odyssey Imager (LI-COR, Lincoln, NE, USA) or Image J.

RNA Isolation and Quantitative RT-PCR (qPCR)

Total RNA was extracted by using the traditional Trizol method (Invitrogen). Quantitative gene expression was performed by two-step quantitative RT-PCR using iScript cDNA Synthesis Kits (cat# 170–8891, Bio-Rad) and SYBR Green PCR Master Mix (Applied Biosystems) with QuantStudio 5 and 6 Flex Real-Time PCR System. mRNA expression levels were determined using the ΔΔCT method and normalized to the housekeeping genes Rps16 and Rps18. The primers used are listed in Supplementary Table 1.

Statistical Analyses

No statistical methods were used to pre-determine sample sizes, but our sample size is similar to previous publications with similar procedures. Number of experimental repeats or mice (*n*) are indicated in the legends. All results from the representative experiments described in this study were reproduced at least two times in independent experiments. Studies were not performed blinded as mouse genotypes were predetermined. Mice were randomly grouped based on their genotypes for treatments. Mice in the transgenic cohorts who occasionally have malocclusions were excluded from studies, as this affects their nutritional status. Two sample in the lipidomics analysis of sWAT was excluded due to sample loss. All data were expressed as mean ±SEM. Data distribution was assumed to be normal but this was not formally tested. For two independent data sets, two-tailed unpaired Student's *t*-test was used. For multiple comparisons, one-way or two-way ANOVA were used followed by Holm-Sidak post hoc test. The statistical analyses were performed with GraphPad Prism 8.0 (GraphPad Software, Inc. La Jolla, CA, USA).

Extended Data

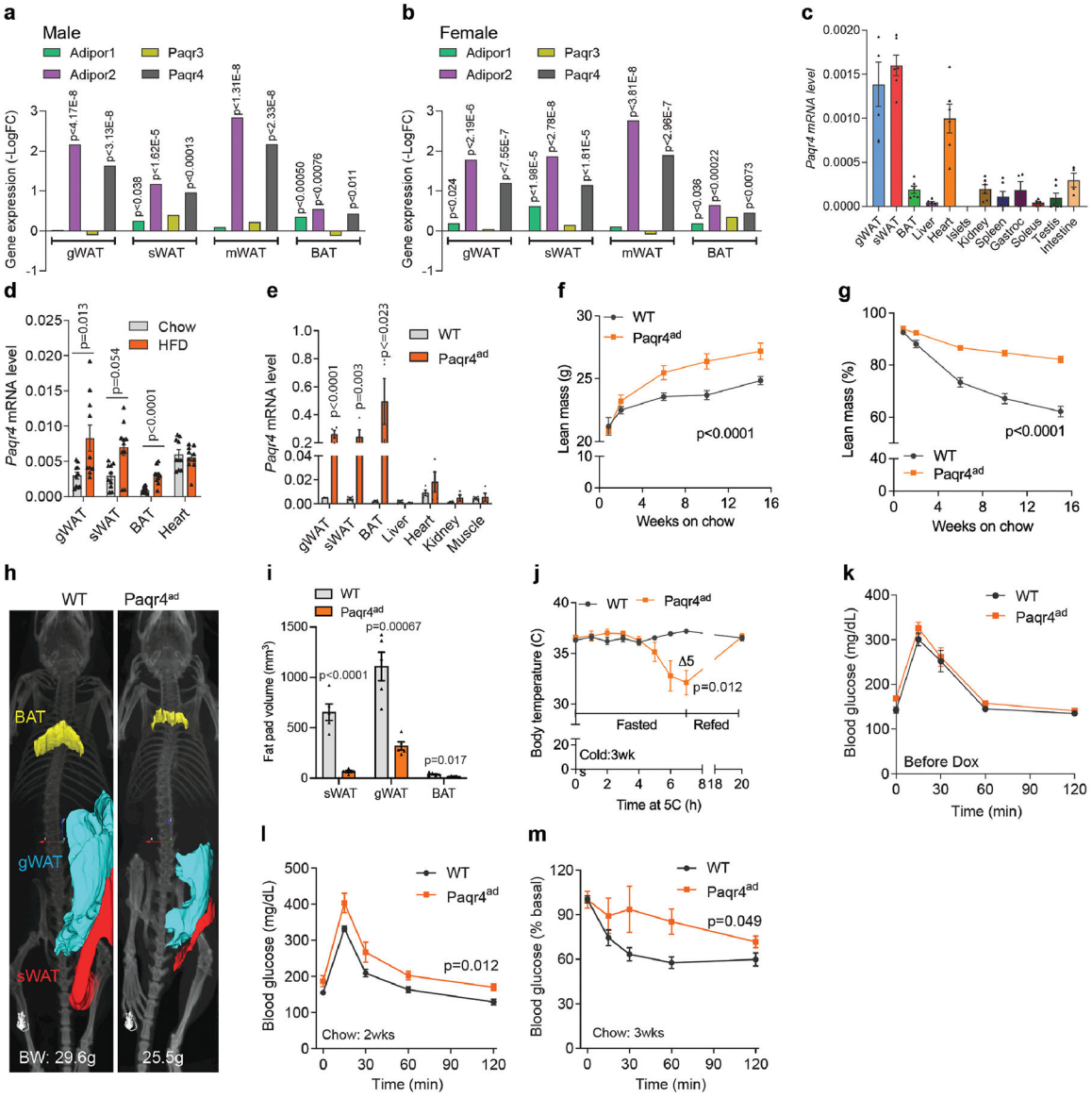

Extended Data Fig.1.

PAQR4 is an important player in regulating adipose tissue function

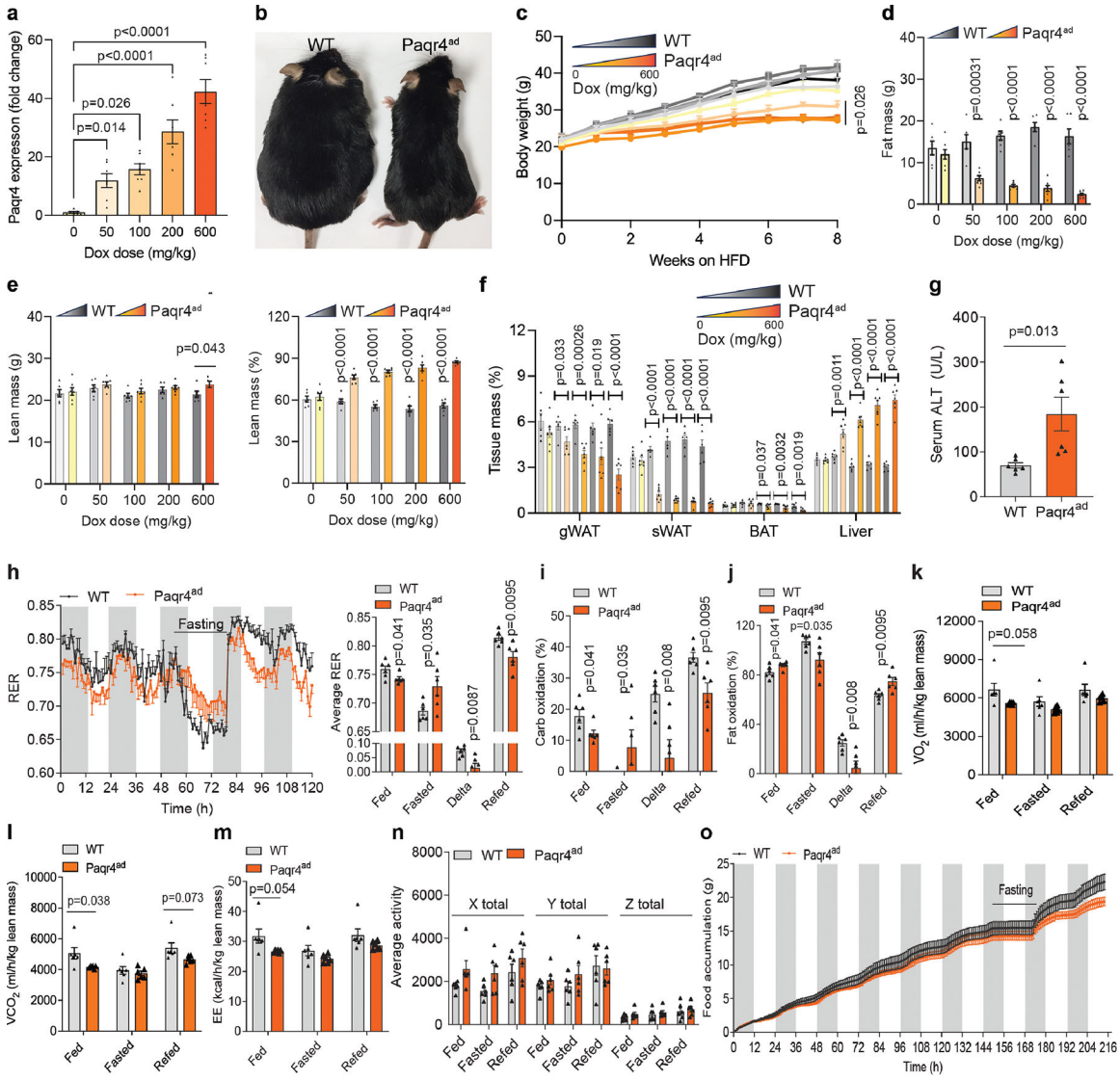

Extended Data Fig. 2.

Pagr4 overexpressing in adipocytes reduced weight gain upon HFD-feeding

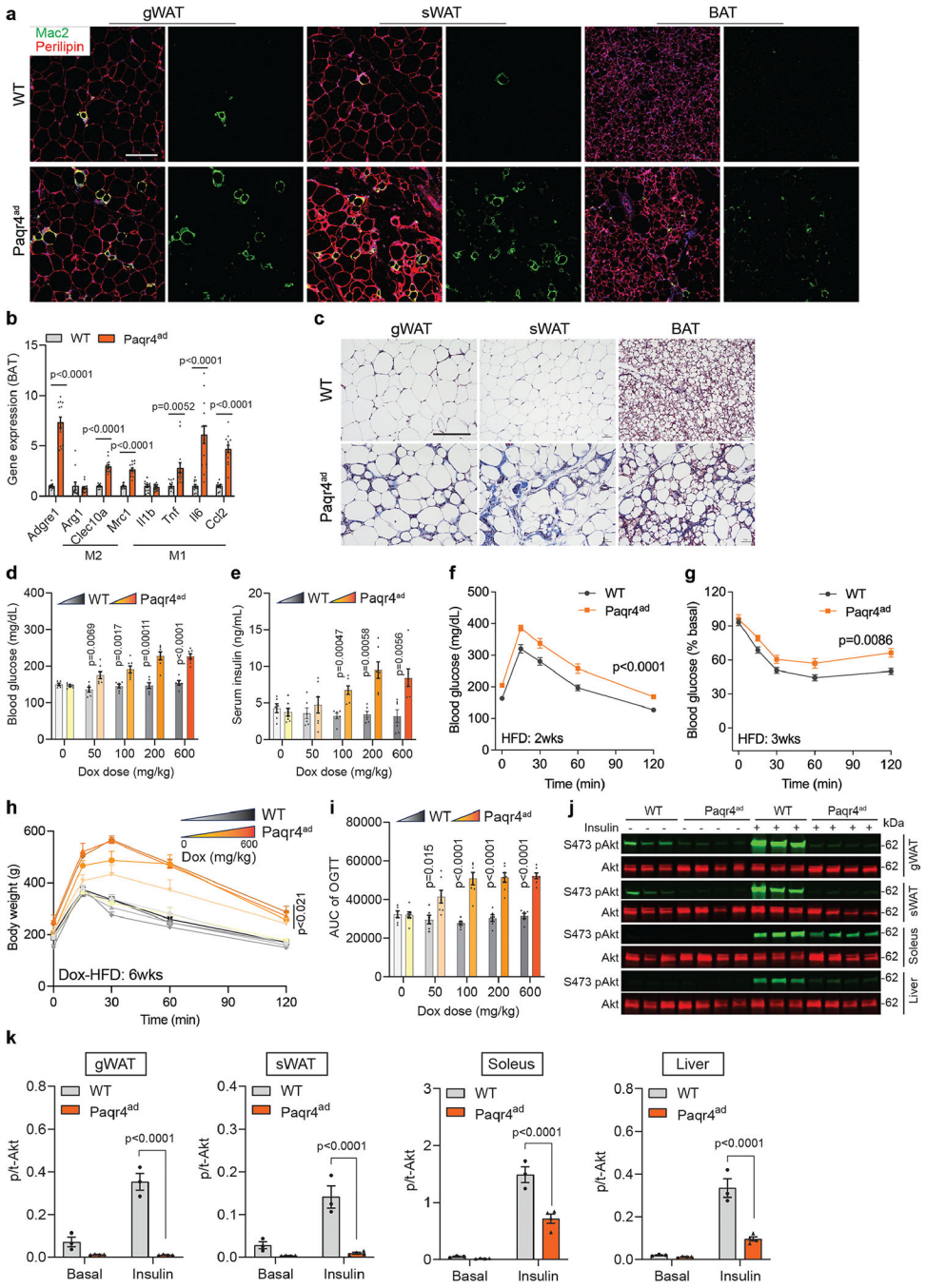

Extended Data Fig. 3.

Paqr4 overexpressing in adipocytes induces insulin resistance upon HFD-feeding

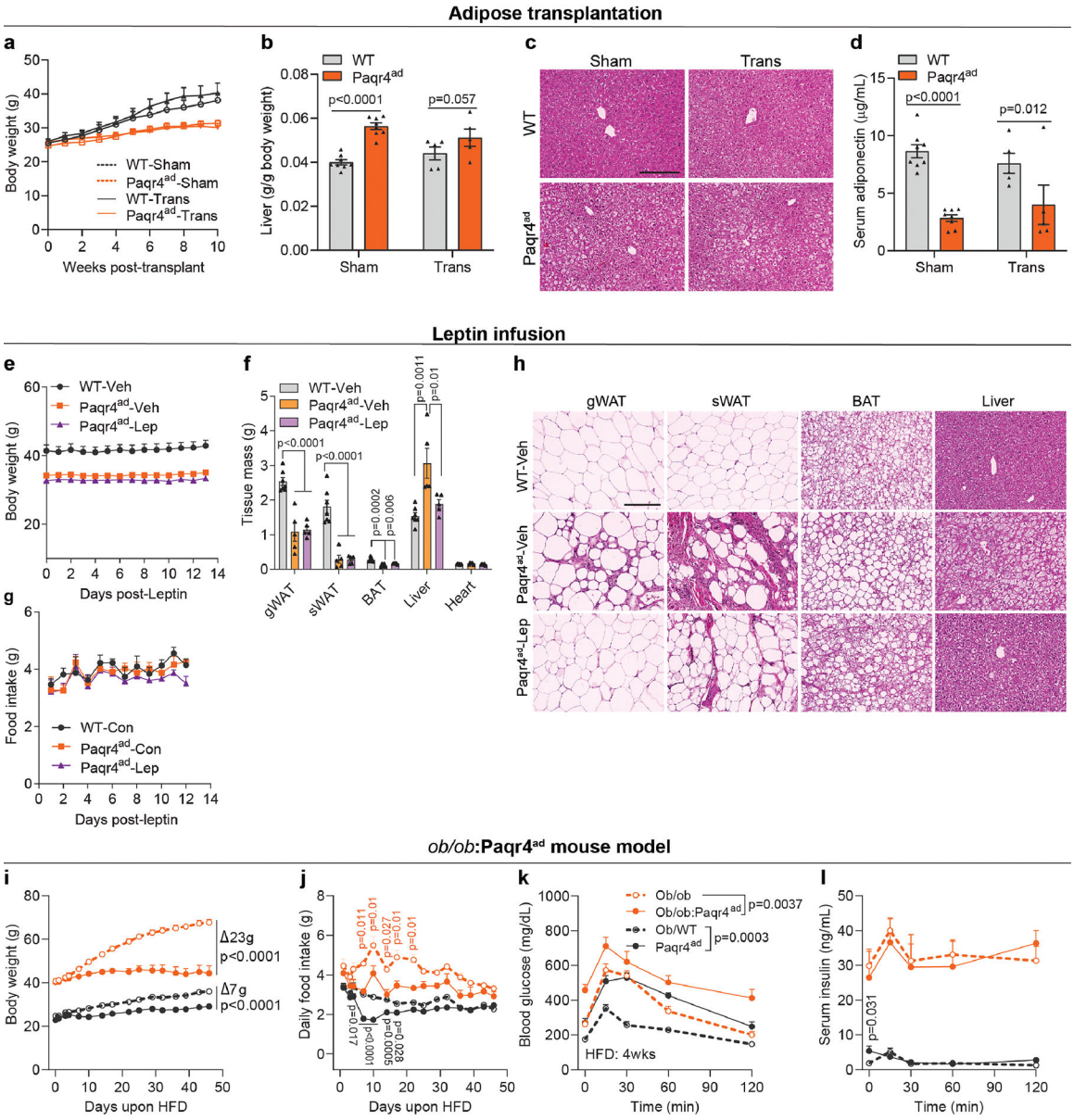

Extended Data Fig. 4.

Amelioration of PAQR4-induced metabolic defects by adipose transplants or leptin treatment

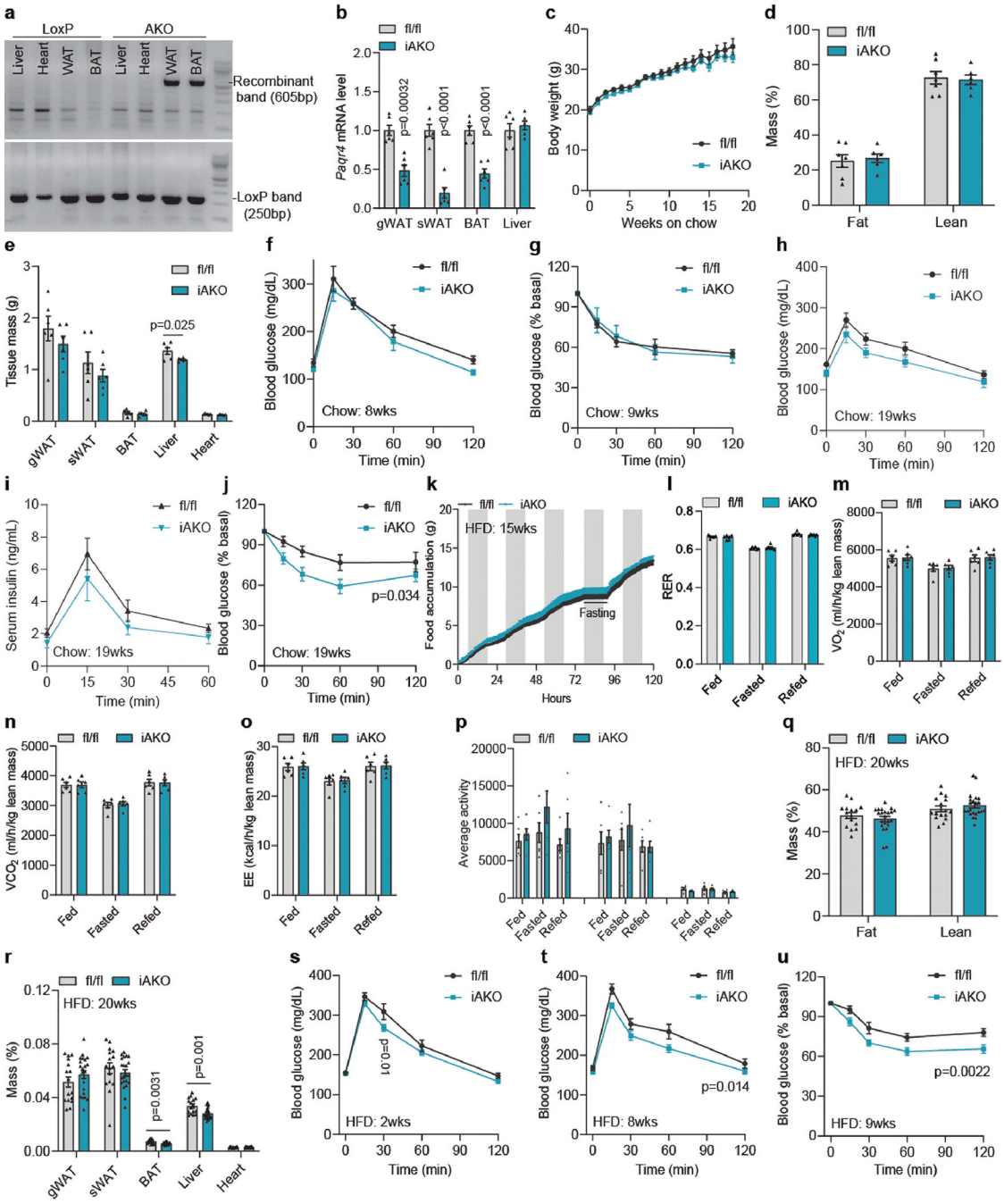

Extended Data Fig. 5.

Adipocyte-specific deletion of *Paqr4* improves glucose homeostasis in obesity

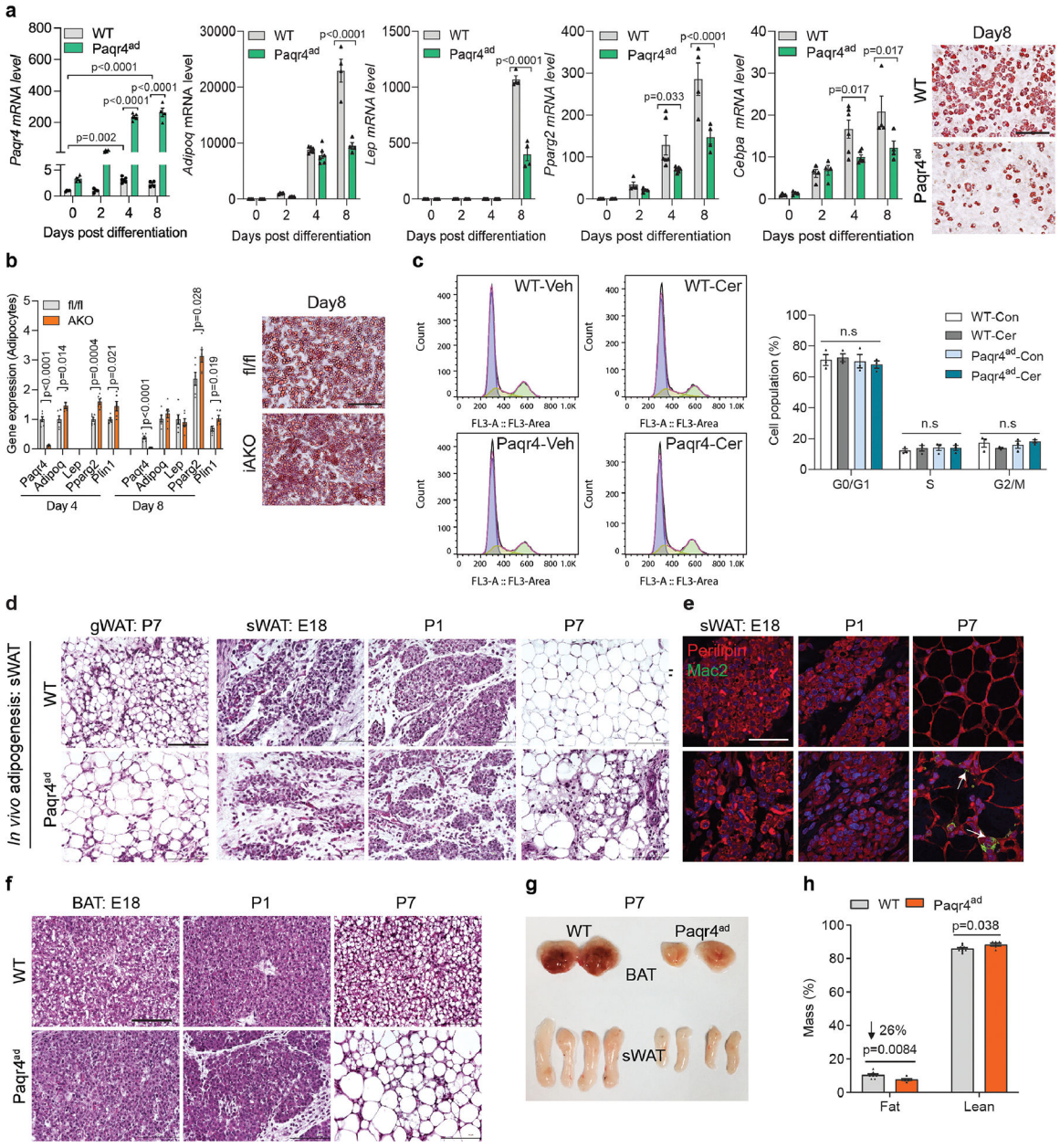

Extended Data Fig. 6.
PAQR4 suppresses adipogenesis

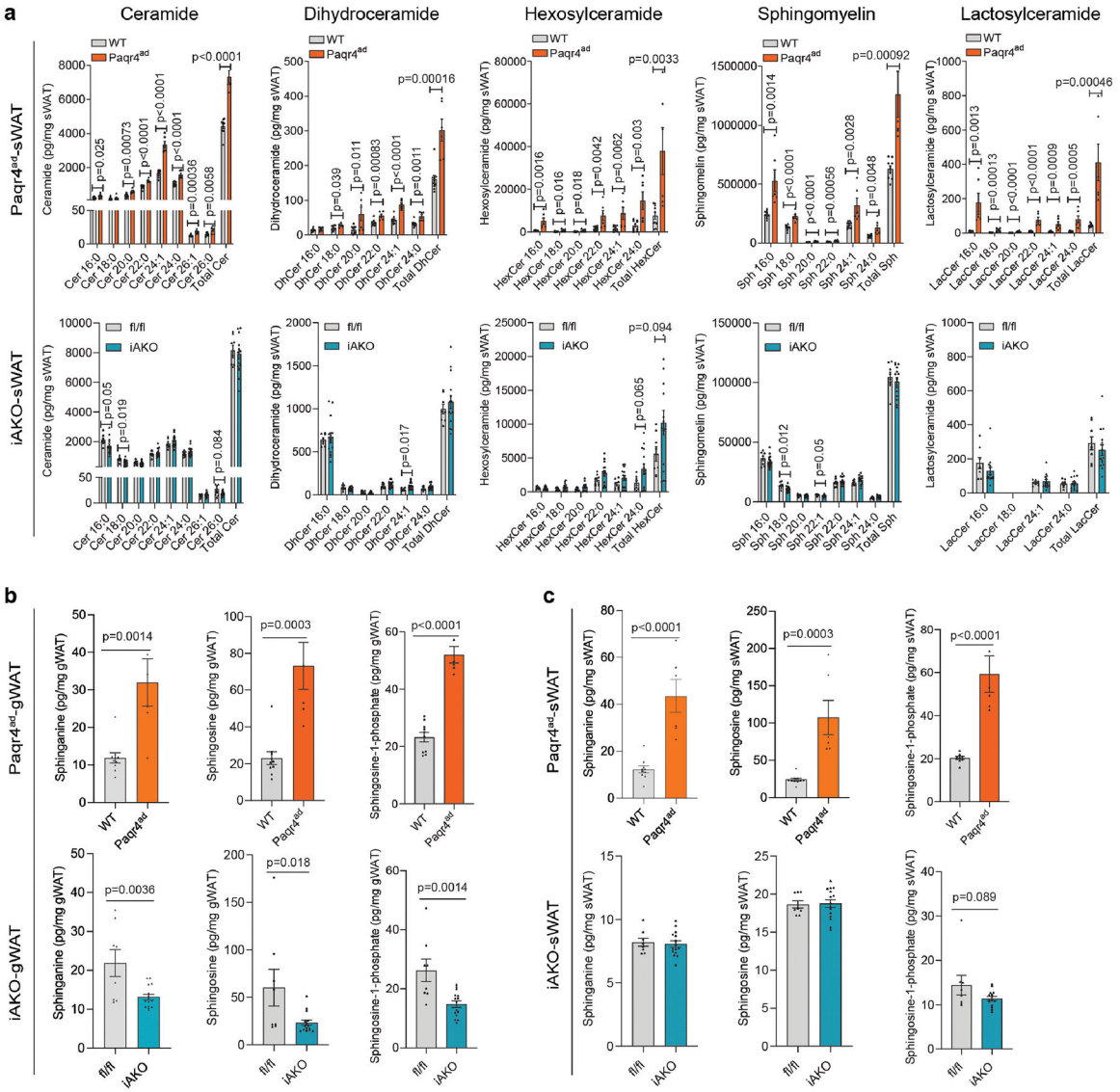

Extended Data Fig. 7.

Effects of PAQR4 on sphingolipid levels in adipose tissues

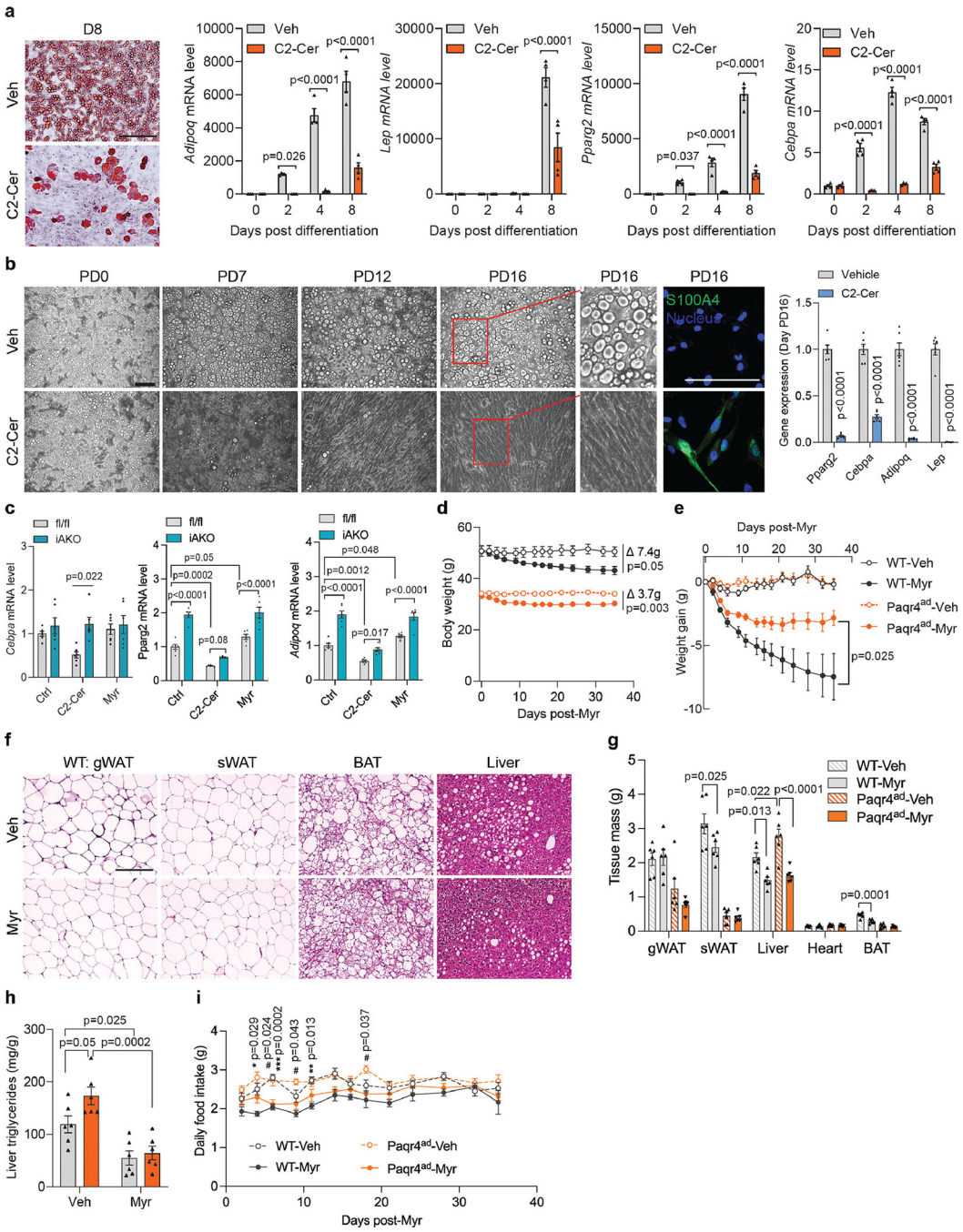

Extended Data Fig.8.

Blocking ceramide synthesis improves PAQR4-induced metabolic defects

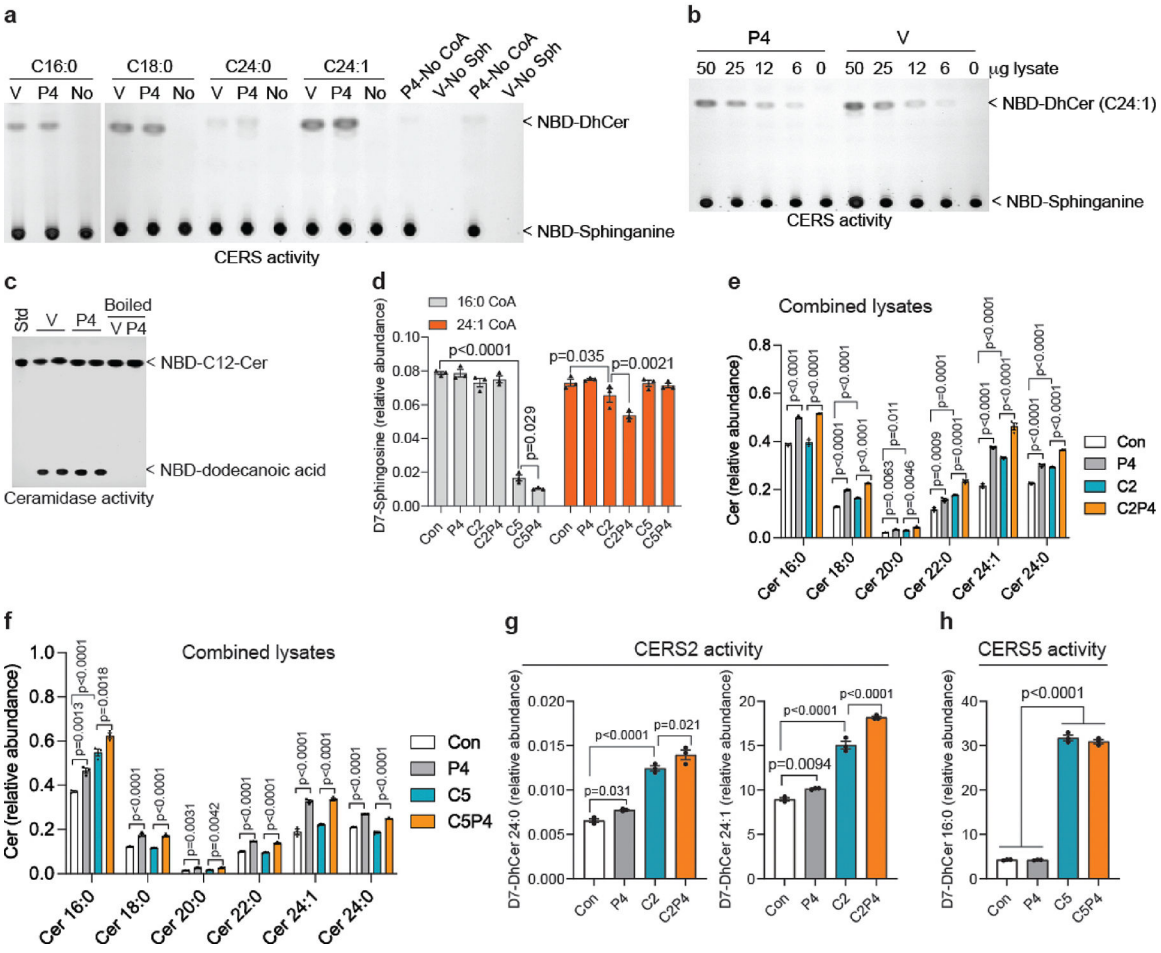

Extended Data Fig.9.

PAQR4 regulates ceramide synthase activity

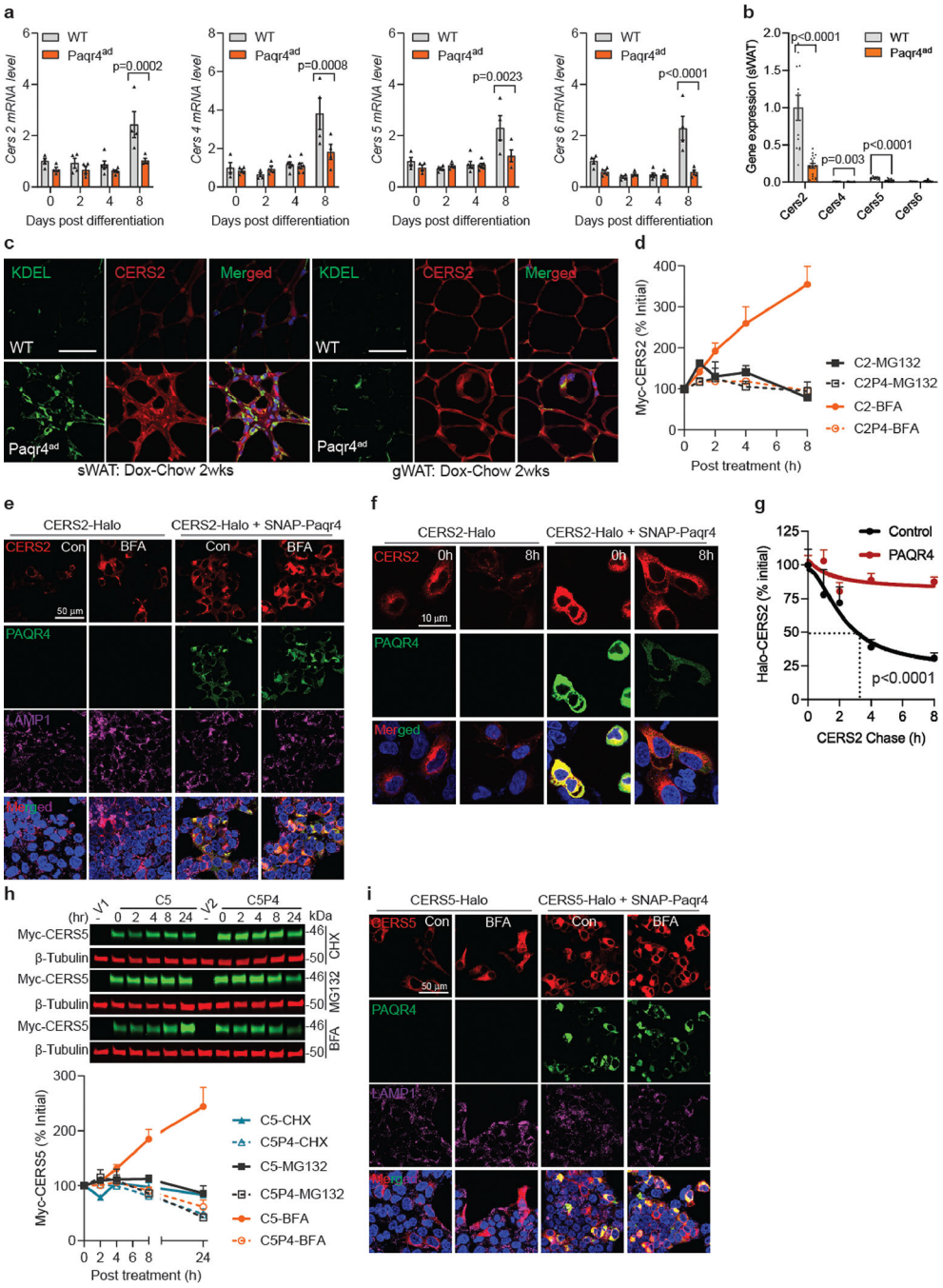

Extended Data Fig.10.
PAQR4 promotes ceramide synthase stability

Supplementary Material

Refer to Web version on PubMed Central for supplementary material.

Acknowledgments

We thank the UTSW Animal Resource Center, Histology Core, Metabolic Phenotyping Core, the Live Cell Imaging Core, Transgenic Core, Proteomics Core and Flow Cytometry Facility for their excellent assistance with experiments performed here. We thank Helmholtz Zentrum München for the generation of Paqr4-flox mouse. We also thank Shimadzu Scientific Instruments for the collaborative efforts in mass spectrometry technology resources. This study was supported by US NIH grants RC2-DK118620, R01-DK55758, R01-DK099110, R01-DK127274, P01 AG051459 and R01-DK131537 to P.E.S., as well as NIDDK-NORC P30-DK127984; NIH grant R00-AG068239 to S.Z., DFG Walter Benjamin Fellowship 444933586 to L.G.S. and AHA Career Development Award 855170 to Q.Z.

Data availability

ScRNA-seq data is accessible in Gene Expression Omnibus (GSE246712). All other data from this study are available with this paper including source data which are provided.

References

1. Zhu Q & Scherer PE Immunologic and endocrine functions of adipose tissue: implications for kidney disease. Nature Reviews Nephrology vol. 14 105–120 (2018). [PubMed: 29199276]
2. Zhu Q, An YA & Scherer PE Mitochondrial regulation and white adipose tissue homeostasis. Trends Cell Biol. 32, 351–364 (2022). [PubMed: 34810062]
3. Wang QA et al. Reversible de-differentiation of mature white adipocytes into preadipocyte-like precursors during lactation. Cell Metab. 28, 282–288.e3 (2018). [PubMed: 29909970]
4. Zhang Z et al. Dermal adipose tissue has high plasticity and undergoes reversible dedifferentiation in mice. J. Clin. Invest. 129, 5327–5342 (2019). [PubMed: 31503545]
5. Shook BA et al. Dermal adipocyte lipolysis and myofibroblast conversion are required for efficient skin repair. Cell Stem Cell 26, 880–895.e6 (2020). [PubMed: 32302523]
6. Bi P et al. Notch activation drives adipocyte dedifferentiation and tumorigenic transformation in mice. J. Exp. Med. 213, 2019–2037 (2016). [PubMed: 27573812]
7. Liu SC et al. Epstein-barr virus induces adipocyte dedifferentiation to modulate the tumor microenvironment. Cancer Res. 81, 3283–3294 (2021). [PubMed: 33824135]
8. Zhu Q et al. Adipocyte mesenchymal transition contributes to mammary tumor progression. Cell Rep. 40, (2022).
9. Chaurasia B et al. Adipocyte ceramides regulate subcutaneous adipose browning, inflammation, and metabolism. Cell Metab. 24, 820–834 (2016). [PubMed: 27818258]
10. Scherer PE The many secret lives of adipocytes: implications for diabetes. Diabetologia 62, 223–232 (2019). [PubMed: 30465066]
11. Turpin-Nolan SM & Brüning JC The role of ceramides in metabolic disorders: when size and localization matters. Nat. Rev. Endocrinol. 16, 224–233 (2020). [PubMed: 32060415]
12. Chaurasia B et al. Targeting a ceramide double bond improves insulin resistance and hepatic steatosis. Science (80-.). 365, 386–392 (2019).
13. Kupchak BR, Garitaonandia I, Villa NY, Smith JL & Lyons TJ Antagonism of human adiponectin receptors and their membrane progesterone receptor paralogs by TNFα and a ceramidase inhibitor. Biochemistry 48, 5504–5506 (2009). [PubMed: 19453184]
14. Tang YT et al. PAQR proteins: A novel membrane receptor family defined by an ancient 7-transmembrane pass motif. J. Mol. Evol. 61, 372–380 (2005). [PubMed: 16044242]
15. Yamauchi T, Iwabu M, Okada-iwabu M & Kadowaki T Adiponectin receptors : A review of their structure , function and how they work. Best Pract. Res. Clin. Endocrinol. Metab. 28, 15–23 (2014). [PubMed: 24417942]
16. Holland WL et al. Receptor-mediated activation of ceramidase activity initiates the pleiotropic actions of adiponectin. Nat. Med. 17, 55–63 (2011). [PubMed: 21186369]
17. Garitaonandia I, Smith JL, Kupchak BR & Lyons TJ Adiponectin identified as an agonist for PAQR3/RKTG using a yeast-based assay system. J. Recept. Signal Transduct. 29, 67–73 (2009).

18. Pedersen L et al. Golgi-localized PAQR4 mediates antiapoptotic ceramidase activity in breast cancer. Cancer Res. 80, 2163–2174 (2020). [PubMed: 32291319]
19. Xu D et al. PAQR3 modulates cholesterol homeostasis by anchoring Scap/SREBP complex to the Golgi apparatus. Nat. Commun. 6, (2015).
20. Jiang Y et al. Functional cooperation of RKTG with p53 in tumorigenesis and epithelial-mesenchymal transition. Cancer Res. 71, 2959–2968 (2011). [PubMed: 21385899]
21. Yu X, Li Z, Chan MTV & Wu WKK PAQR3: A novel tumor suppressor gene. Am. J. Cancer Res. 5, 2562–2568 (2015). [PubMed: 26609468]
22. Zhang H et al. PAQR4 has a tumorigenic effect in human breast cancers in association with reduced CDK4 degradation. Carcinogenesis 39, 439–446 (2018). [PubMed: 29228296]
23. Okada-Iwabu M et al. A small-molecule AdipoR agonist for type 2 diabetes and short life in obesity. Nature 503, 493–499 (2013). [PubMed: 24172895]
24. Beals JW et al. Increased Adipose Tissue Fibrogenesis, Not Impaired Expandability, Is Associated With Nonalcoholic Fatty Liver Disease. Hepatology 74, 1287–1299 (2021). [PubMed: 33743554]
25. Kusminski CM et al. MitoNEET-driven alterations in adipocyte mitochondrial activity reveal a crucial adaptive process that preserves insulin sensitivity in obesity. Nat. Med. 18, 1539–1551 (2012). [PubMed: 22961109]
26. An YA et al. The mitochondrial dicarboxylate carrier prevents hepatic lipotoxicity by inhibiting white adipocyte lipolysis. J. Hepatol. 75, 387–399 (2021). [PubMed: 33746082]
27. Ferrero R, Rainer P & Deplancke B Toward a Consensus View of Mammalian Adipocyte Stem and Progenitor Cell Heterogeneity. Trends Cell Biol. 30, 937–950 (2020). [PubMed: 33148396]
28. Burl RB et al. Deconstructing Adipogenesis Induced by β3-Adrenergic Receptor Activation with Single-Cell Expression Profiling. Cell Metab. 28, 300–309.e4 (2018). [PubMed: 29937373]
29. Merrick D et al. Identification of a mesenchymal progenitor cell hierarchy in adipose tissue. Science (80-.). 364, aav2501 (2019).
30. Schwalie PC et al. A stromal cell population that inhibits adipogenesis in mammalian fat depots. Nature 559, 103–108 (2018). [PubMed: 29925944]
31. Shao M et al. Pathologic HIF1α signaling drives adipose progenitor dysfunction in obesity. Cell Stem Cell 28, 685–701.e7 (2021). [PubMed: 33539723]
32. Wang QA, Tao C, Gupta RK & Scherer PE Tracking adipogenesis during white adipose tissue development, expansion and regeneration. Nat. Med. 19, 1338–1344 (2013). [PubMed: 23995282]
33. Ussher JR et al. Inhibition of de novo ceramide synthesis reverses diet-induced insulin resistance and enhances whole-body oxygen consumption. Diabetes 59, 2453–2464 (2010). [PubMed: 20522596]
34. Amrutkar M et al. Genetic disruption of protein kinase STK25 ameliorates metabolic defects in a diet-induced type 2 diabetes model. Diabetes 64, 2791–2804 (2015). [PubMed: 25845663]
35. Guerre-Millo M et al. PPAR-α-null mice are protected from high-fat diet-induced insulin resistance. Diabetes 50, 2809–2814 (2001). [PubMed: 11723064]
36. Xia JY et al. Targeted induction of ceramide degradation leads to improved systemic metabolism and reduced hepatic steatosis. Cell Metab. 22, 266–278 (2015). [PubMed: 26190650]
37. Ogretmen B Sphingolipid metabolism in cancer signalling and therapy. Nat. Rev. Cancer 18, 33–50 (2017). [PubMed: 29147025]
38. Spalding KL et al. Dynamics of fat cell turnover in humans. Nature 453, 783–787 (2008). [PubMed: 18454136]
39. Ghaben AL & Scherer PE Adipogenesis and metabolic health. Nat. Rev. Mol. Cell Biol. 20, 242–258 (2019). [PubMed: 30610207]
40. Sprott KM, Chumley MJ, Hanson JM & Dobrowsky RT Decreased activity and enhanced nuclear export of CCAAT-enhancer-binding protein β during inhibition of adipogenesis by ceramide. Biochem.J 181–191 (2002).
41. Wang QA, Tao C, Gupta RK & Scherer PE Tracking adipogenesis during white adipose tissue development, expansion and regeneration. Nat. Med. 19, 1338–1344 (2013). [PubMed: 23995282]
42. Jones JEC et al. The adipocyte acquires a fibroblast-like transcriptional signature in response to a high fat diet. Sci. Rep. 10, 1–15 (2020). [PubMed: 31913322]

43. Roh HC et al. Adipocytes fail to maintain cellular identity during obesity due to reduced PPARγ activity and elevated TGFβ-SMAD signaling. Mol. Metab. 42, 101086 (2020). [PubMed: 32992037]
44. Kruglikov IL & Scherer PE Dermal adipocytes: from irrelevance to metabolic targets? Trends Endocrinol. Metab. 27, 1–10 (2016). [PubMed: 26643658]
45. Shan B et al. Perivascular mesenchymal cells control adipose-tissue macrophage accrual in obesity. Nat. Metab. 2, 1332–1349 (2020). [PubMed: 33139957]
46. Laviad EL, Kellys S, Merrill AH & Futerman AH Modulation of ceramide synthase activity via dimerization. J. Biol. Chem. 287, 21025–21033 (2012). [PubMed: 22539345]
47. Hammerschmidt P et al. CerS6-derived sphingolipids interact with Mff and promote mitochondrial fragmentation in obesity. Cell 177, 1536–1552.e23 (2019). [PubMed: 31150623]
48. Raichur S et al. CerS2 haploinsufficiency inhibits β-oxidation and confers susceptibility to diet-induced steatohepatitis and insulin resistance. Cell Metab. 20, 687–695 (2014). [PubMed: 25295789]
49. Rodriguez-Cuenca S, Pellegrinelli V, Campbell M, Oresic M & Vidal-Puig A Sphingolipids and glycerophospholipids – The “ying and yang” of lipotoxicity in metabolic diseases. Prog. Lipid Res. 66, 14–29 (2017). [PubMed: 28104532]
50. Volkmar N et al. Regulation of membrane fluidity by RNF145 -triggered degradation of the lipid hydrolase ADIPOR2 . EMBO J. 41, 1–22 (2022).
51. Wang K et al. Pan-cancer analysis of the prognostic and immunological role of PAQR4. Sci. Rep. 12, 1–16 (2022). [PubMed: 34992227]
52. Brachtendorf S, El-Hindi K & Grösch S Ceramide synthases in cancer therapy and chemoresistance. Prog. Lipid Res. 74, 160–185 (2019). [PubMed: 30953657]
53. Morad SAF & Cabot MC Ceramide-orchestrated signalling in cancer cells. Nat. Rev. Cancer 13, 51–65 (2013). [PubMed: 23235911]
54. Li Y et al. Ceramides Increase Fatty Acid Utilization in Intestinal Progenitors to Enhance Stemness and Increase Tumor Risk. Gastroenterology 1–15 (2023) doi:10.1053/j.gastro.2023.07.017.
55. Zhang Y et al. C24-ceramide drives gallbladder cancer progression through directly targeting phosphatidylinositol 5-phosphate 4-kinase type-2 gamma to facilitate mammalian target of rapamycin signaling activation. Hepatology 73, 692–712 (2021). [PubMed: 32374916]
56. Dany M & Ogretmen B Ceramide induced mitophagy and tumor suppression. Biochim. Biophys. Acta - Mol. Cell Res. 1853, 2834–2845 (2015).
57. Inoue T et al. Mechanistic insights into the hydrolysis and synthesis of ceramide by neutral ceramidase. J. Biol. Chem. 284, 9566–9577 (2009). [PubMed: 19088069]
58. Okino N et al. The reverse activity of human acid ceramidase. J. Biol. Chem. 278, 29948–29953 (2003). [PubMed: 12764132]
59. El Bawab S et al. Biochemical characterization of the reverse activity of rat brain ceramidase. A CoA-independent and fumonisin B1-insensitive ceramide synthase. J. Biol. Chem. 276, 16758–16766 (2001). [PubMed: 11278489]
60. Zhu Q et al. Suppressing adipocyte inflammation promotes insulin resistance in mice. Mol. Metab. 39, 1–11 (2020).
61. Deng Y et al. Adipocyte Xbp1s overexpression drives uridine production and reduces obesity. Mol. Metab. 11, 1–17 (2018). [PubMed: 29551634]
62. Zhang Z et al. Adipocyte iron levels impinge on a fat-gut crosstalk to regulate intestinal lipid absorption and mediate protection from obesity. Cell Metab. 33, 1624–1639.e9 (2021). [PubMed: 34174197]
63. Zhu Q et al. Adipocyte-specific deletion of Ip6k1 reduces diet-induced obesity by enhancing AMPK-mediated thermogenesis. J. Clin. Invest. 126, 4273–4288 (2016). [PubMed: 27701146]
64. Zhang Z et al. Insulin resistance and diabetes caused by genetic or diet-induced KBTBD2 deficiency in mice. Proc. Natl. Acad. Sci. U. S. A. 113, E6418–E6426 (2016). [PubMed: 27708159]

65. Kusminski CM et al. A novel model of diabetic complications: Adipocyte mitochondrial dysfunction triggers massive β-cell hyperplasia. Diabetes 69, 313–330 (2020). [PubMed: 31882562]

66. Rampler E et al. Simultaneous non-polar and polar lipid analysis by on-line combination of HILIC, RP and high resolution MS. Analyst 143, 1250–1258 (2018). [PubMed: 29431763]

67. Kim HJ, Qiao Q, Toop HD, Morris JC & Don AS A fluorescent assay for ceramide synthase activity. J. Lipid Res. 53, 1701–1707 (2012). [PubMed: 22661289]

68. Tani M, Okino N, Mitsutake S & Ito M Specific and sensitive assay for alkaline and neutral ceramidases involving C12-NBD-ceramide. J. Biochem. 125, 746–749 (1999). [PubMed: 10101288]

69. Zhu Q, Ghoshal S, Tyagi R & Chakraborty A Global IP6K1 deletion enhances temperature modulated energy expenditure which reduces carbohydrate and fat induced weight gain. Mol. Metab. 6, 73–85 (2017). [PubMed: 28123939]

70. Ninagawa S et al. Forcible destruction of severely misfolded mammalian glycoproteins by the non-glycoprotein ERAD pathway. J. Cell Biol. 211, 775–784 (2015). [PubMed: 26572623]

71. Zhang Y et al. C24-Ceramide Drives Gallbladder Cancer Progression Through Directly Targeting Phosphatidylinositol 5-Phosphate 4-Kinase Type-2 Gamma to Facilitate Mammalian Target of Rapamycin Signaling Activation. Hepatology 73, 692–712 (2021). [PubMed: 32374916]

Highlights

- PAQR4 regulates ceramide levels by mediating ceramide synthase stability and activity.
- PAQR4 overactivity causes ceramide accumulation, reduces adipogenesis and promotes adipocyte de-differentiation.
- Overexpression of *Paqr4* in adipocytes causes partial lipodystrophy and systemic metabolic dysfunction, which is ameliorated by blocking *de novo* ceramide biosynthesis.
- Deletion of *Paqr4* in adipocytes reduces adipose ceramide levels and improves healthy adipose tissue remodeling and insulin sensitivity in obesity.

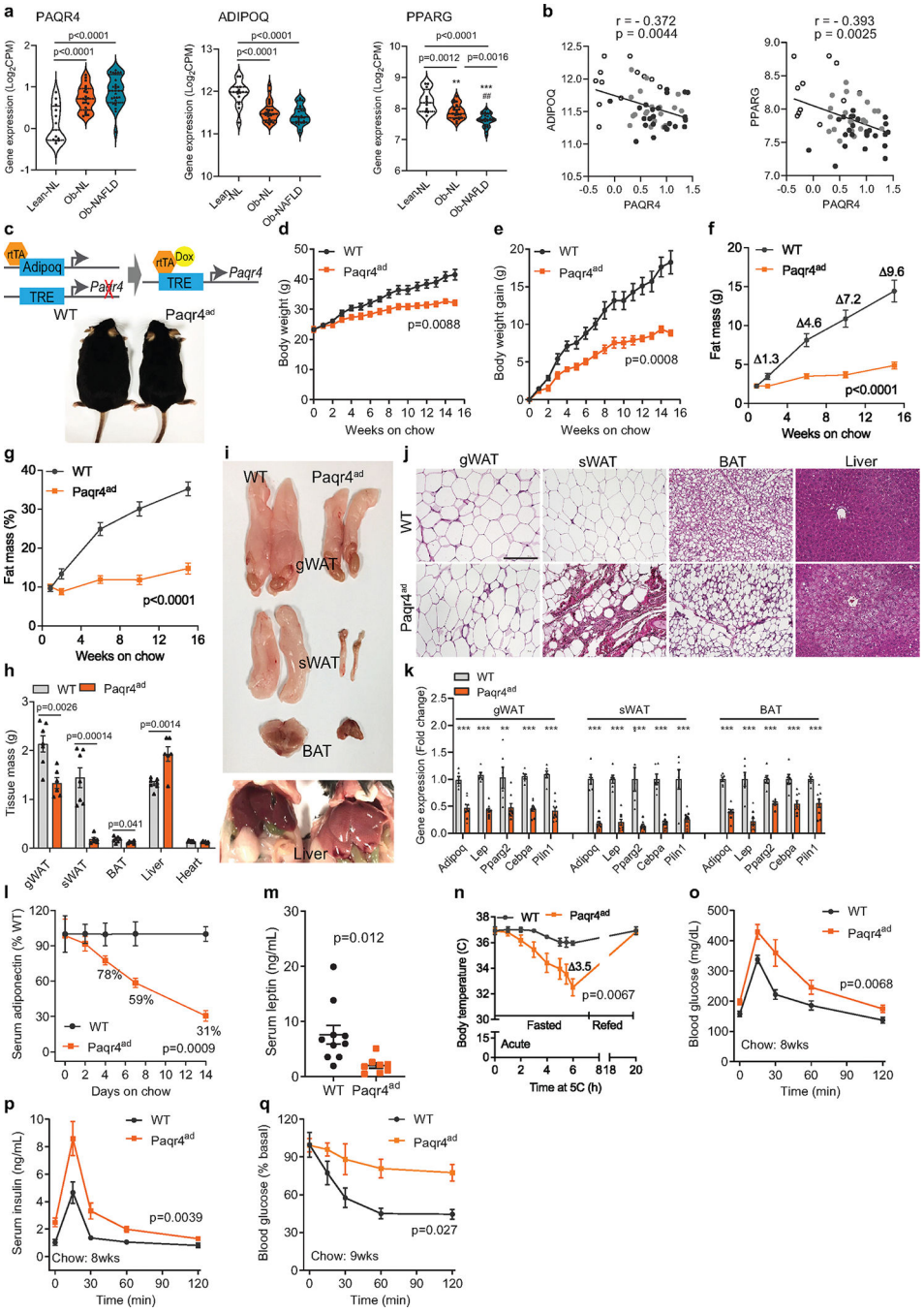

Fig. 1. PAQR4 is an important player in regulating adipose tissue function.

(**a**) Gene expression of *PAQR4*, *ADIPOQ* and *PPARG* from human abdominal sWAT. Data extracted from GSE159924. Lean-NL, healthy lean normal, n=12; Ob-NL, obese with normal intrahepatic triglyceride content and normal glucose tolerance, n=21; Ob-NAFLD, obese with NAFLD and abnormal glucose metabolism, n=24. (**b**) Inversely correlation of gene expression of *PAQR4* with adipocyte markers *ADIPOQ* and *PPARG*. Individual data represent Lean-NL (white cycles), Ob-NL (grey cycles) and Ob-NAFLD (dark cycles). (**c**) Scheme of Paqr4^{ad} mouse model (top); Paqr4^{ad} mice are leaner (bottom) fed dox-chow diet

for 15 weeks. (**d**-**h**) Reduced body weight and weight gain (WT, n=7; Paqr4^{ad}, n=6), reduced fat mass and fat percentage (WT, n=8; Paqr4^{ad}, n=10), reduced fat pad weights and elevated liver weights (WT, n=7; Paqr4^{ad}, n=6) in Paqr4^{ad} mice fed dox-chow diet for 15 weeks. (**i**) Smaller fat pads and fatty liver in Paqr4^{ad} mice. (**j**) H&E staining of adipose tissues and liver (WT, n=3; Paqr4^{ad}, n=4). Scale bar 200 μm. (**k**) Down-regulation of mature adipocyte markers in different adipose tissues from Paqr4^{ad} mice fed dox-chow diet for one week (WT, n=6; Paqr4^{ad}, n=9). (**l**) Progressive reduction of serum adiponectin levels in Paqr4^{ad} mice fed with dox-chow diet (n=5). (**m**) Reduced serum leptin levels in Paqr4^{ad} mice fed dox-chow diet for one week (WT, n=10; Paqr4^{ad}, n=8). (**n**) Paqr4^{ad} mice display hypothermia upon acute cold exposure under fasting conditions fed dox-chow diet for 2 weeks (WT, n=7; Paqr4^{ad}, n=6). (**o**-**q**) Impaired glucose tolerance, glucose-stimulated hyperinsulinemia, and insulin-mediated glucose disposal in Paqr4^{ad} mice fed dox-chow diet for 8–9 weeks (WT, n=7; Paqr4^{ad}, n=6). Data shown as mean ± SEM and analyzed by two-way ANOVA (**d**-**g**, **l**, **n**-**q**), one-way ANOVA followed by Holm-Sidak multiple-comparison test (**a**), Person correlation test (**b**), and two-tailed unpaired *t*-test (**k**, **m**).

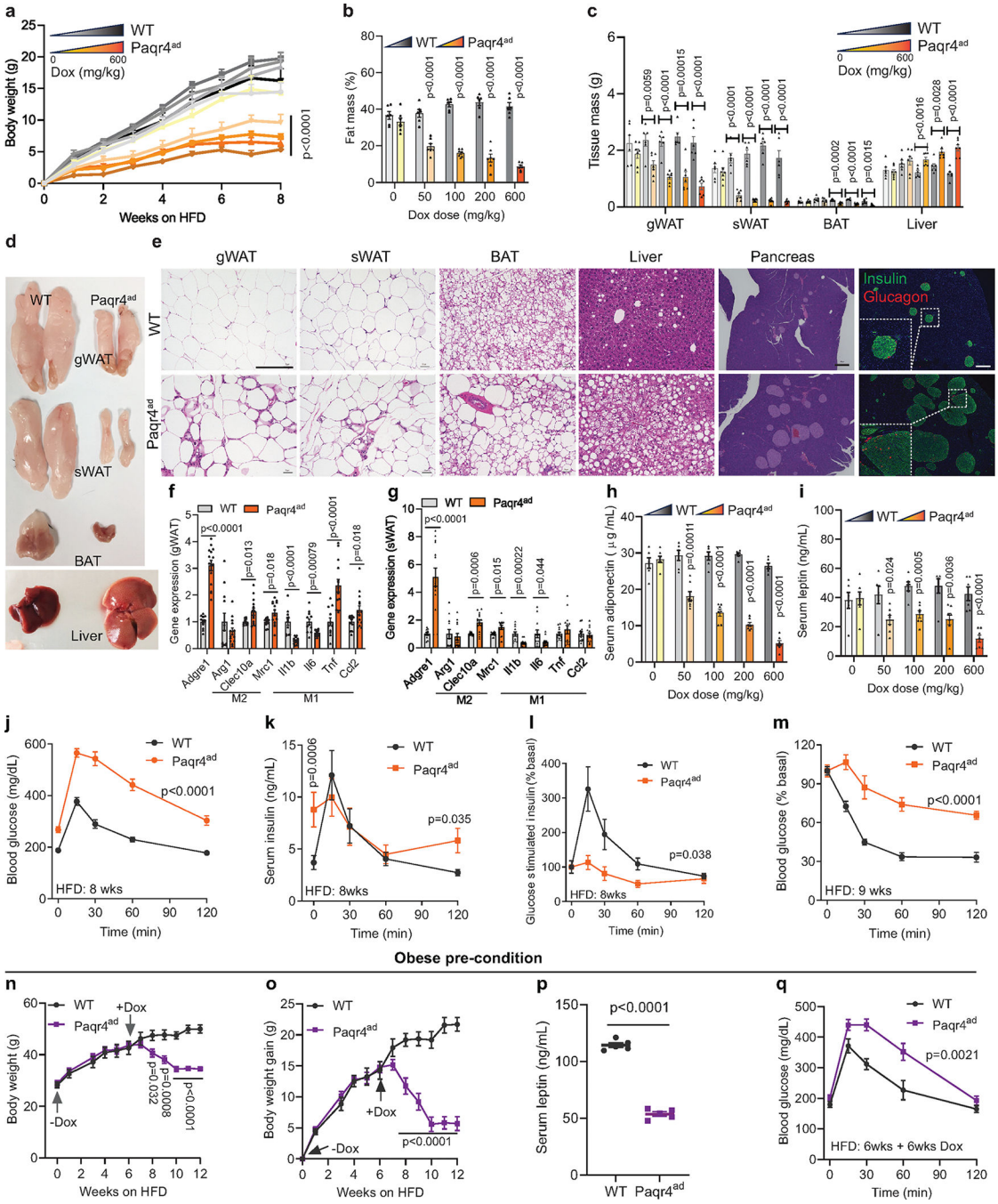

Fig. 2. *Paqr4* overexpressing mice display insulin resistance despite reduced weight upon HFD-feeding.

Mice were fed dox-HFD (600mg/kg except in the dox-response assays). (**a-c**) Dox-dose dependent effects on reduction in weight gain, fat percentage, fat pad weights, and liver weight in Paqr4^{ad} mice at week 8 (WT, n=6; Paqr4^{ad}, n=7). (**d**) Smaller fat pads and fatty liver in Paqr4^{ad} mice. (**e**) H&E staining of adipose tissues, liver, and pancreas and immunostaining of insulin (green) and glucagon (red) of pancreas (n=3). Scale bar for adipose tissues and liver 200 μm; for pancreas 400 μm. (**f-g**) Inflammatory gene expressions

in gWAT and sWAT at week 3 (WT, n=12; Paqr4^{ad}, n=14). (**h-i**) Dox-dose response effects of reduction in serum adiponectin and leptin levels in Paqr4^{ad} mice WT, n=6; Paqr4^{ad}, n=7). (**j-l**) Impaired glucose tolerance (WT, n=14; Paqr4^{ad}, n=12) and glucose-stimulated insulin release (n=6) in Paqr4^{ad} mice. (**m**) Impaired insulin-mediated glucose disposal in Paqr4^{ad} mice (WT, n=8; Paqr4^{ad}, n=6). (**n-q**) Reduced body weight and weight gain, decreased serum leptin levels on week 2, and impaired glucose tolerance on week 6 upon switching to dox-HFD in obese Paqr4^{ad} mice priorly fed 6 weeks of HFD without dox (n=5). Data shown as mean ± SEM and analyzed by two-way ANOVA (**a, j-o**, **q**) and two-tailed unpaired *t*-test (**b-c**, **f-i**, **p**).

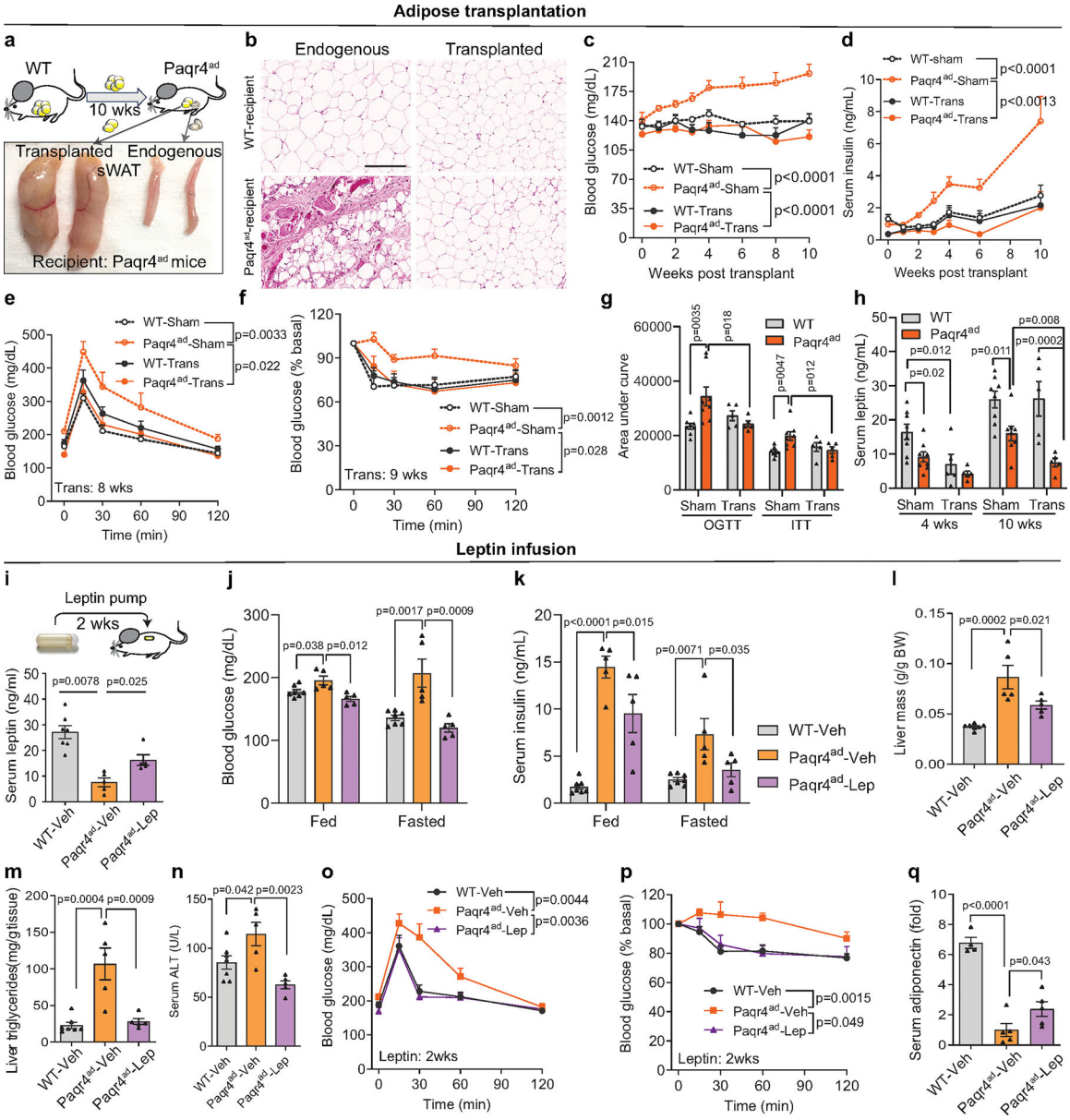

Fig. 3. Amelioration of PAQR4-induced metabolic dysfunction with adipose tissue transplants or leptin administration.

Mice receiving subcutaneous adipose tissue transplants (sWAT) were fed dox-chow for 10 weeks. (**a**) Endogenous and transplanted sWAT in Paqr4^{ad} mice. (**b**) Transplanted sWAT displays healthy morphology in both WT and Paqr4^{ad} mice (n=3). Scale bar 200 μm. (**c-g**) Adipose transplant normalizes hyperglycemia, hyperinsulinemia, glucose tolerance, and insulin-mediated glucose disposal in Paqr4^{ad} mice (Sham, n=8 per group; Transplant, n=5 per group). (**h**) Adipose transplant does not recover serum leptin in Paqr4^{ad} mice (Sham, n=8 per group; Transplant, n=5 per group). (**i**) Two weeks of leptin infusion increases serum leptin levels in Paqr4^{ad} mice that were previously exposed to dox-chow for 14 weeks (WT, n=7; Paqr4^{ad}, n=5 per group). (**j-k**) Leptin improves hyperglycemia and hyperinsulinemia in Paqr4^{ad} mice (WT, n=7; Paqr4^{ad}, n=5 per group). (**l-n**) Leptin reduces liver/body weight

ratio, liver triglyceride content, and serum ALT levels in Paqr4^{ad} mice (WT, n=7; Paqr4^{ad}, n=5 per group). (**o-p**) Leptin normalizes glucose tolerance and insulin-mediated glucose disposal in Paqr4^{ad} mice (WT, n=7; Paqr4^{ad}, n=5 per group). (**q**) Leptin slightly increases serum adiponectin levels in Paqr4^{ad} mice (WT, n=4; Paqr4^{ad}, n=5 per group). Data shown as mean ± SEM and analyzed by two-way ANOVA (**c-h, o-p**) and one-way ANOVA followed by Holm-Sidak multiple-comparison test (**i-n**, **q**).

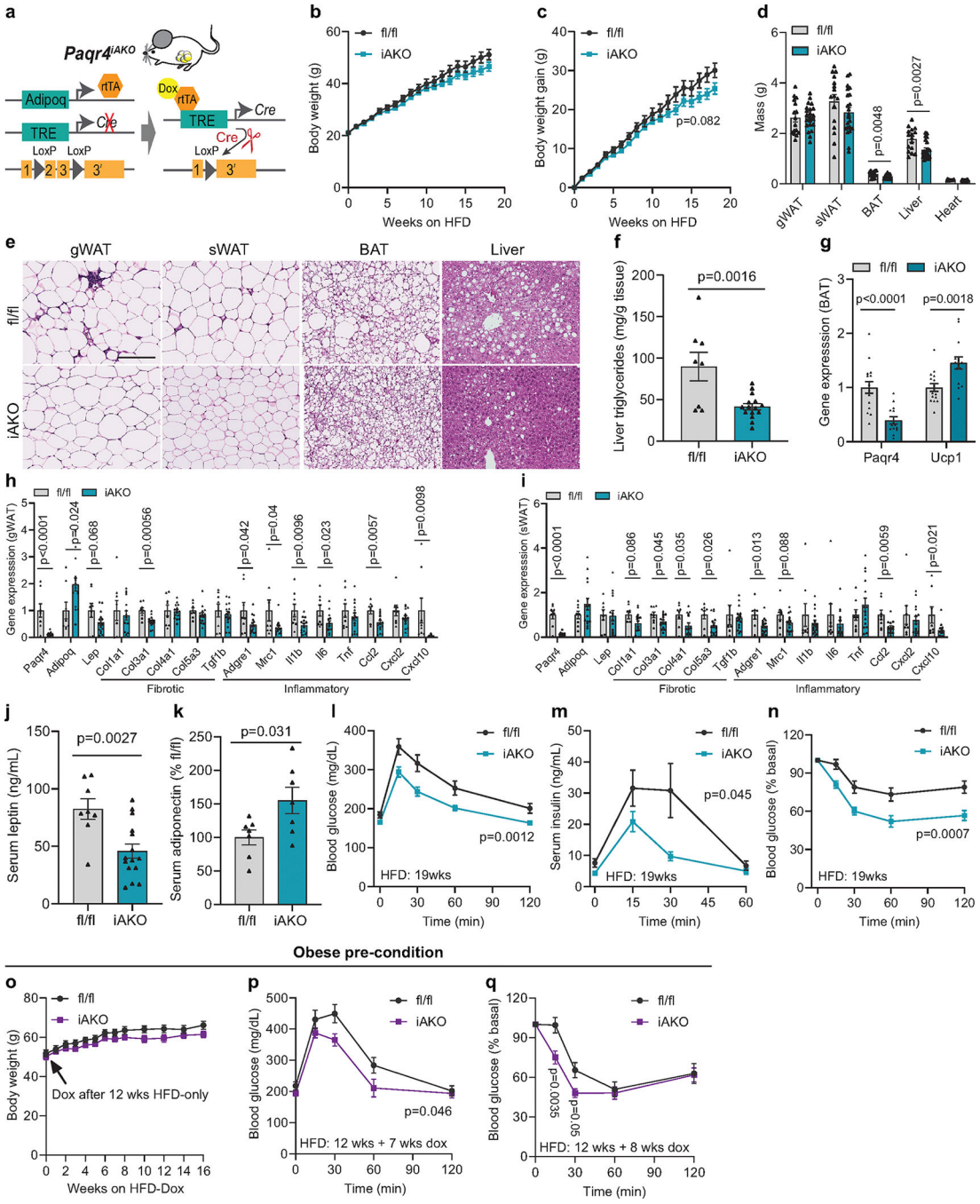

Fig. 4. Adipocyte-specific deletion of *Paqr4* improves glucose homeostasis in obesity.

Mice were fed dox-HFD. (**a**) Scheme of Paqr4^{iAKO} mouse model. (**b-c**) Body weight and weight gain upon dox-HFD feeding (Paqr4$^{fl/fl}$, n=16; Paqr4^{iAKO}, n=22). (**d**) Tissue weight at week 20 (Paqr4$^{fl/fl}$, n=16; Paqr4^{iAKO}, n=22). (**e**) H&E staining of adipose tissues and liver (n=6). Scale bar 200 μm. (**f**) Reduced liver triglyceride content in Paqr4^{iAKO} mice (Paqr4$^{fl/fl}$, n=8; Paqr4^{iAKO}, n=15). (**g**) Up-regulation of *Ucp1* in Paqr4^{iAKO}-BAT (Paqr4$^{fl/fl}$, n=16; Paqr4^{iAKO}, n=14). (**h-i**) Expression of genes related to fibrogenesis and inflammation in gWAT and sWAT (Paqr4$^{fl/fl}$, n=8; Paqr4^{iAKO}, n=15). (**j**) Reduced serum leptin levels in

Paqr4^{iAKO} mice (Paqr4$^{fl/fl}$, n=8; Paqr4^{iAKO}, n=15). (**k**) Elevated serum adiponectin levels in Paqr4^{iAKO} mice (n=7). (**l-n**) Improved glucose tolerance and enhanced insulin-mediated glucose disposal (Paqr4$^{fl/fl}$, n=16; Paqr4^{iAKO}, n=22) with less glucose-stimulated insulin secretion (n=15) in Paqr4^{iAKO} mice. (**o-p**) Deletion of *Paqr4* in obese preconditioned mice improves glucose tolerance and insulin-mediated glucose disposal without affecting body weight (Paqr4$^{fl/fl}$, n=7; Paqr4^{iAKO}, n=8). Data shown as mean and analyzed by two-way ANOVA (**b-c, l-q**) and two-tailed unpaired *t*-test (**d, f-k**).

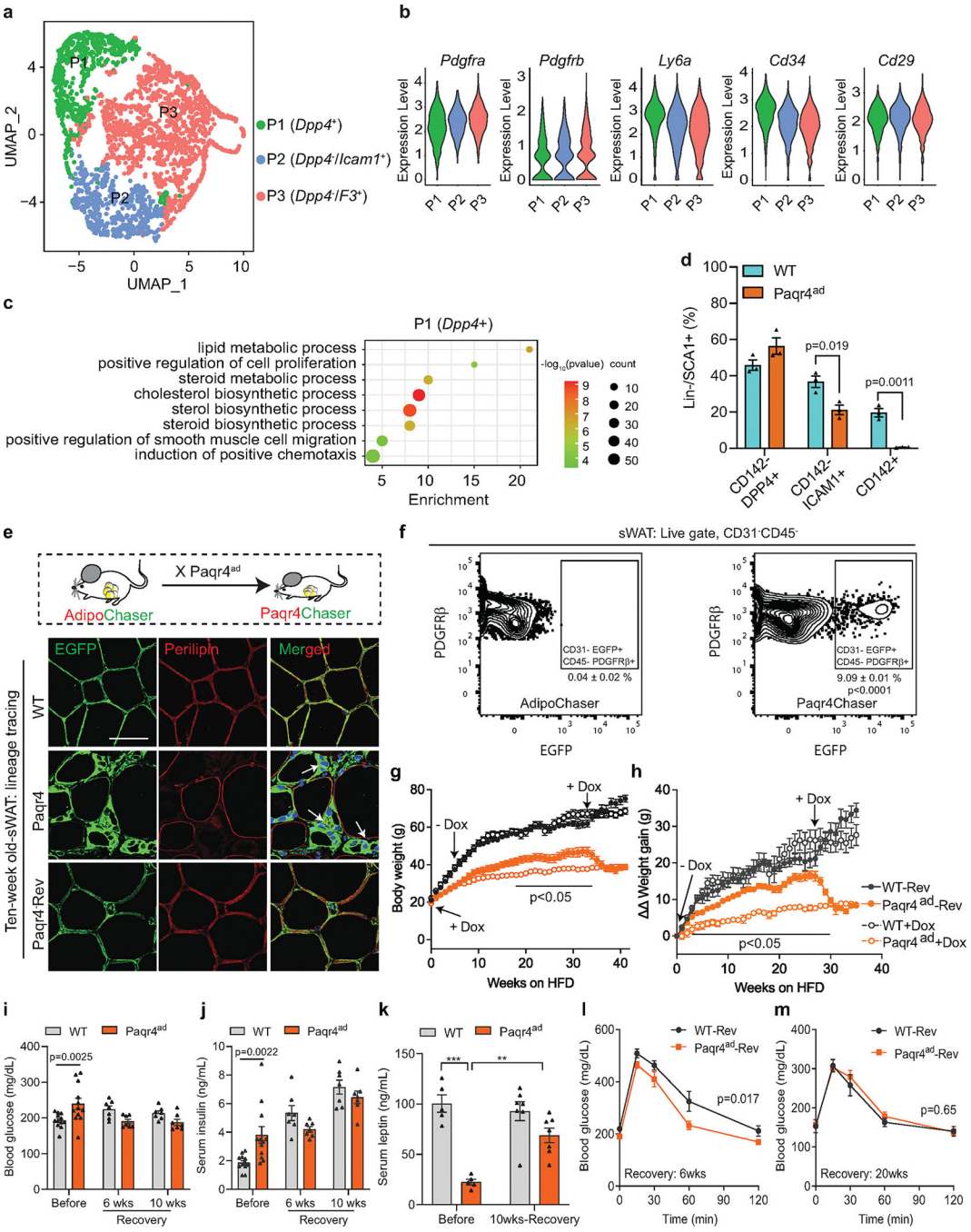

Fig. 5. PAQR4 promotes adipose remodeling and adipocyte de-differentiation.

(**a**) Aggregated UMAP plot of subcutaneous adipose stem and progenitor cells (ASPCs) from WT and Paqr4^{ad} mice. ASPCs were grouped into three subpopulations P1 (*Dpp4*+), P2 (*Icam1*+), and P3 (*F3*+). (**b**) ASPCs were identified based on well-established ASPC gene markers. The y axis is the log-scale normalized read count. (**c**) Gene ontology (GO) pathways related to biological processes with differentially expressed genes in P1 (*Dpp4*+) subpopulation between genotypes. p<0.001, FDR < 0.05. (**d**) Cell frequency of ASPCs in sWAT analyzed by flow cytometry (n=3 mice per group). (**e**) Immunofluorescent staining

of Perilipin (red) and EGFP (green) in sWAT (n=3) from Paqr4Chaser and control mice. Eight-week-old chaser mice were fed dox-chow for 2 weeks and then allowed to recover on dox-free chow for 4 weeks. Scale bar 50 μm. (**f**) Flow cytometry analysis of sWAT-SVF cells from Paqr4Chaser mice indicates adipocyte de-differentiated into PDGFRβ^{+} precursor cells (n=3 biological samples). (**g**-**h**) Body weight and ΔΔ weight gain during dox-recovery (Rev). ΔΔ weight gain represents body weight minus respective Δ weight gain; Δ weight gain represents body weight minus respective body weight at start point of dox-withdrawal. (Dox, n=5 for each group; Rev, n=7 for each group). *p*-values indicate comparisons between groups of Paqr4^{ad}-Rev and Paqr4^{ad}+Dox. The arrows indicated dox-intervention in the dox-recovery groups. (**i**-**k**) Blood glucose, serum insulin (before, n=12 for each group; Recovery, n=7 for each group), and serum leptin (before, n=5 for each group; Recovery, n=7 for each group) during dox-recovery. (**l**-**m**) Glucose tolerance tests during dox-recovery (n=7). Data shown as mean ± SEM and analyzed by two-way ANOVA (**g**-**m**) and two-tailed unpaired *t*-test (**d**, **f**).

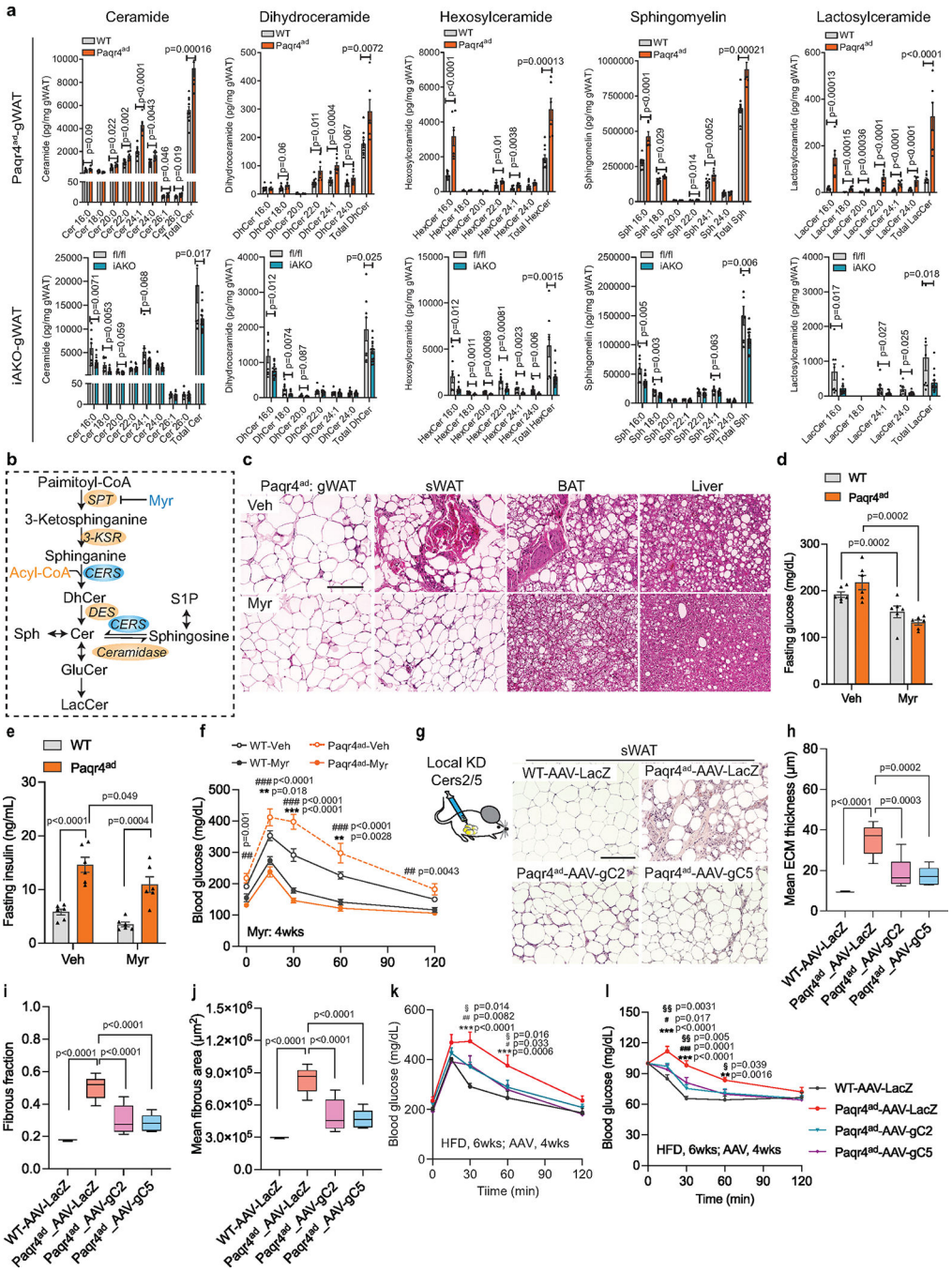

Fig. 6. Blocking ceramide *de novo* biosynthesis improves PAQR4-induced metabolic dysfunction.

(**a**) Sphingolipids are largely elevated in Paqr4^{ad}-gWAT (WT, n=10; Paqr4^{ad}, n=6) and decreased in Paqr4^{iAKO}-gWAT (Paqr4$^{fl/fl}$, n=8; Paqr4^{iAKO}, n=15) upon dox-HFD feeding. (**b**) Sphingolipid metabolic pathway. (**c**) H&E staining of adipose tissues and liver after 5 weeks of vehicle (Veh) or myriocin (Myr) treatment (Vehicle, n=3; Myr, n=4). Scale bar 200 μm. (**d-f**) Myr improves hyperglycemia, hyperinsulinemia, and glucose tolerance 4 weeks post-treatment (n=6). For (f), * indicates comparisons between groups of WT-Veh and Paqr4^{ad}-Veh; $^{\#}$ indicates comparisons between groups of Paqr4^{ad}-Veh and Paqr4^{ad}-Myr.

(**g**-**j**) Local knockdown of *Cers2* (C2) or *Cers5* (C5) via targeted CRISPR gRNAs using Adeno-associated virus (AAV) improves local adipose tissue fibrosis in Paqr4^{ad} mice. Mice were beforehand fed HFD without dox for two weeks, and then received local injection of AAVs in inguinal fat pads; mice were then switched to dox-HFD 2 weeks post-AAV injections. Fibrosis was analyzed from histological images from (g) (n=3 for WT; N=7 for other groups). (**k**-**l**) Glucose tolerance and insulin tolerance tests 4 weeks post-AAV injections (n=7 for each group). * indicates comparisons between groups of WT-AAV-LacZ and Paqr4^{ad}-AAV-LacZ; $^{\#}$ and § indicate comparisons between groups of Paqr4^{ad}-AAV-LacZ and Paqr4^{ad}-AAV-gC2 or Paqr4^{ad}-AAV-gC5, respectively. Data shown as mean ± SEM or in Boxplots (line, median; whiskers, minima to maxima) and analyzed by two-way ANOVA (**d**-**f, k**-**l**), one-way ANOVA followed by Holm-Sidak multiple-comparison test (**h**-**j**), and two-tailed unpaired *t*-test (**a**).

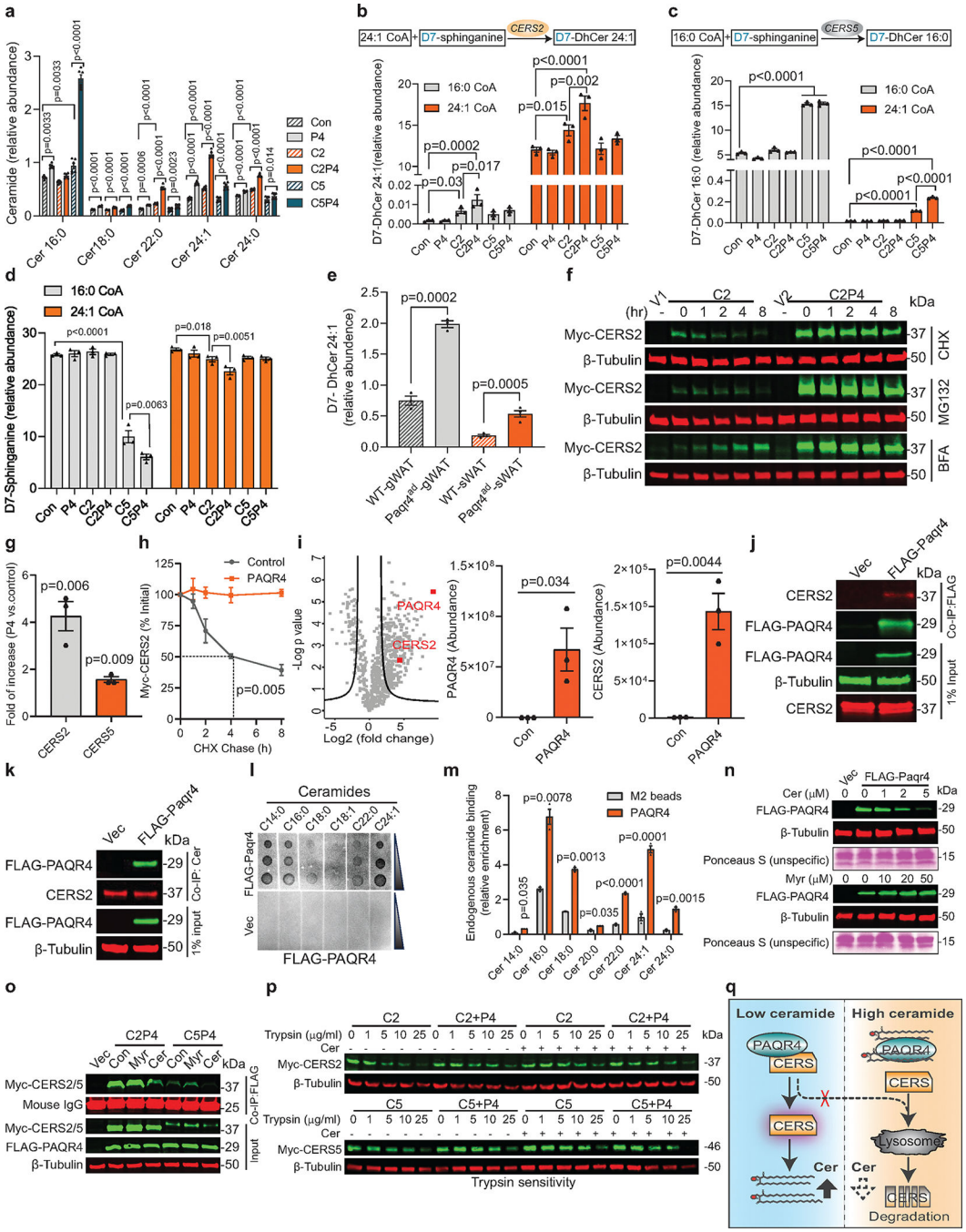

Fig. 7. PAQR4 regulates ceramide levels by mediating ceramide synthase activity.

(**a**) PAQR4 (P4) increases CERS2 (C2)/CERS5 (C5)-induced ceramide levels, as measured in lysates with overexpression of P4, C2, and C5 alone or in combination in HEK293T cells (n=3 biological samples). (**b-c**) Enzymatic activities of CERS2/5 are determined from (a) using stable isotope labeled D7-sphinganine (n=3 biological samples). (**d**) Consumption of D7-sphinganine (n=3 biological samples). (**e**) CERS2 activity in adipose microsomes (gWAT, n=3; sWAT, n=4 per group). (**f**) CERS2 protein levels in presence of cycloheximide (CHX), MG132, or bafilomycin A1 (BFA) (n=3). (**g**) PAQR4 increases CERS2/5 protein

levels in HEK293T cells (n=3 biological samples). (**h**) PAQR4 increases CERS2 stability (n=3 independent assays with similar results). (**i**) Unbiased proteomics identified CERS2 as a PAQR4 interactor in adipocytes (n=3 biological samples). (**j**) PAQR4 binds CERS2 in adipocytes. Representative blots from 2 independent assays with similar results. (**k**) Ceramides bind CERS2 and PAQR4. Representative blots from 2 independent assays with similar results. (**l**) PAQR4 binds exogenous ceramides. (**m**) PAQR4 binds endogenous ceramides. FLAG-PAQR4 was pulled down from HEK293T lysates, total lipids were extracted and bound ceramides were measured by LC-MS/MS. (n=3 biological samples). (**n**) C2-Ceramide (Cer) reduces, whereas myriocin (Myr) increases PAQR4 levels in HEK293T cells (n=4). (**o**) PAQR4 interacts with CERS2/5, which are stabilized by myriocin but diminished by C2-Ceramide (n=3). (**p**) Ceramides affect the binding of PAQR4 with CERS2/5. Individual PAQR4 or CERS2/5 overexpressing lysates were combined and treated with ceramides before trypsin digestion (n=2). (**q**) Proposed model of PAQR4 in the regulation of ceramide levels. At low ceramide levels, PAQR4 binds and stabilizes CERS, thus promoting CERS activity to recover ceramide levels; at high ceramide levels, ceramides bind PAQR4, causing it to dissociate from the PAQR4/CERS complex, resulting in the lysosomal degradation of CERS. Data shown as mean ± SEM and analyzed by two-way ANOVA (**h**), one-way ANOVA (**a-d**), and two-tailed unpaired *t*-test (**e**, **g**, **i**, **m**).